Mosher, D.C., Erbacher, J., and Malone, M.J. (Eds.)
Proceedings of the Ocean Drilling Program, Scientific Results Volume 207

15. Compressibility, Permeability, and Stress History of Sediments from Demerara Rise[1]

Matt O'Regan[2] and Kate Moran[2, 3]

ABSTRACT

The stress history, permeability, and compressibility of sediments from Demerara Rise recovered during Ocean Drilling Program Leg 207 were determined using one-dimensional incremental load consolidation and low-gradient flow pump permeability tests. Relationships among void ratio, effective stress, and hydraulic conductivity are presented for sampled lithologic units and used to reconstruct effective stress, permeability, and in situ void ratio profiles for a transect of three sites across Demerara Rise. Results confirm that a significant erosional event occurred on the northeastern flank of the rise during the late Miocene, resulting in the removal of ~220 m of upper Oligocene–Miocene deposits. Although Neogene and Paleogene sediments tend to be overconsolidated, Cretaceous sediments are normally consolidated to underconsolidated, suggesting the presence of overpressure. A pronounced drop in permeability occurs at the transition from the Cretaceous black shales into the overlying Maastrichtian–upper Paleocene chalks and clays. The development of a hydraulic seal at this boundary may be responsible for overpressure in the Cretaceous deposits, leading to the lower overconsolidation ratios of these sediments. Coupled with large regional variations in sediment thickness (overburden stresses), the higher permeability overpressured Cretaceous sediments represent a regional lateral fluid conduit on Demerara Rise, possibly venting methane-rich fluids where it outcrops on the margin's northeastern flank.

[1] O'Regan, M., and Moran, K., 2007. Compressibility, permeability, and stress history of sediments from Demerara Rise. *In* Mosher, D.C., Erbacher, J., and Malone, M.J. (Eds.), *Proc. ODP, Sci. Results,* 207: College Station, TX (Ocean Drilling Program), 1–35. doi:10.2973/odp.proc.sr.207.114.2007
[2] Graduate School of Oceanography, University of Rhode Island, Narragansett RI, 02882. Correspondence author: **oregan@gso.uri.edu**
[3] Department of Ocean Engineering, University of Rhode Island, Narragansett RI, 02882.

Initial receipt: 4 April 2006
Acceptance: 8 March 2007
Web publication: 16 May 2007
Ms 207SR-114

INTRODUCTION

Fluids play a pivotal role in the dynamics of continental margin evolution. Subseafloor fluids link many physical and chemical processes through the transport of energy and solutes over a wide range of scales. Defining these fluids, their flow systems, controlling mechanisms and rates on both active and passive margins are important scientific questions that have become target themes for the Integrated Ocean Drilling Program (Ge et al., 2002).

In normally consolidated sediments, hydrostatic pressure is maintained in the pore spaces by the expulsion of pore waters as burial compaction progresses. If sediment permeability is sufficiently low or if sedimentation and the accumulation of overburden pressure are sufficiently high (as in many high-productivity shelf environments), pore fluids cannot escape quickly enough and overpressures are generated. In these instances, the retained fluid carries part of the overlying sediment load. As time progresses, pore pressures can reach lithostatic levels and cause fracturing, affect local and regional slope stability, and induce flow channeling (Hart et al., 1995).

On continental margins, downhole variability in formation permeability and horizontal differences in overburden stresses result in the focusing of fluids laterally along preferential flow channels (Dugan and Flemings, 2000). Where these flow channels outcrop on margin flanks, slope instabilities may occur near the seafloor. Modeling on the New Jersey margin has shown that lateral flow along highly permeable Miocene fluid conduits initiates slope failure and feeds cold seeps on the seafloor (Dugan and Flemings, 2000), and similar evidence of mass wasting exists in the Eastern Nankai Trough on the Tokai margin, where active seepage is concentrated along outcrops of coarse turbidites (Henry et al., 2002). In both situations, the margins are characterized by large downhole variations in permeability and lateral heterogeneities in sediment thicknesses.

A similar situation exists on Demerara Rise, an extension of the continental margin off the coasts of French Guyana and Suriname. The rise is covered with 2–3 km of sediment and generally lies <700 meters below sea level (mbsl). Basement rocks on the rise are Precambrian and early Mesozoic and are overlain by pre-Albian synrifted sediments (Erbacher, Mosher, Malone, et al., 2004). The rise's northwestern edge is characterized by a gentle sloping surface that deepens >4000 mbsl while maintaining a generally constant thickness of sediment cover, whereas on the eastern flank, sediments thin in the seaward direction, with basement outcrops occurring below 3500 mbsl.

Five sites drilled on Demerara Rise during Ocean Drilling Program (ODP) Leg 207 constitute a depth transect extending from 1900 to 3200 mbsl. Recovered sediments are primarily Cretaceous and Paleogene deposits defined by five major lithsotratigraphic units (Figs. **F1**, **F2**). Three regional unconformities are identified in the recovered sequences and occur

1. Between the pre-Albian synrifted sediments and the Cenomanian–Santonian black shales,
2. Separating the Cenomanian–Santonian black shale sequence and the overlying Campanian–Paleogene calcareous to siliceous oozes and chalks, and

F1. Leg 207 site map, p. 18.

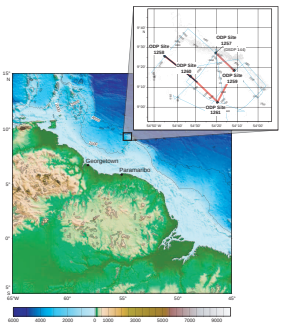

F2. Schematic illustration of age and sediment type, p. 19.

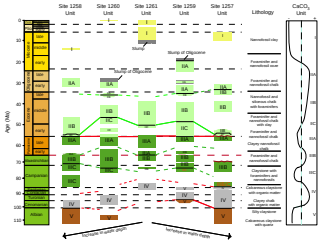

3. Near the late Oligocene–early Miocene, where an erosional surface, formed as part of a short-lived submarine channel system, is thought to be partially responsible for the thin veneer of Neogene deposits on the distal portions of the rise (Erbacher, Mosher, Malone, et al., 2004).

The changing depositional environment on Demerara Rise produced a diverse suite of sediments whose petrophysical properties are complicated by postdepositional diagenetic alterations and periods of erosion or nondeposition. This study presents laboratory test results that describe the permeability, compressibility, and stress history of 12 samples from Sites 1257, 1258, 1259, and 1261 (Fig. F3). The results of laboratory testing allow for the construction of composite effective stress and permeability profiles of the recovered sediments and are used to investigate the timing and magnitude of documented unconformities and the evolution of pore pressure and possible fluid flow regimes on Demerara Rise.

F3. Location and OCR of samples used in this study, p. 20.

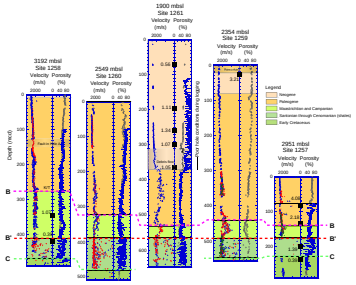

METHODS

Consolidation Tests

One-dimensional incremental load consolidation tests provide key parameters for reconstructing the stress history of clayey marine sediments (Terzaghi, 1943). Testing is performed by incrementally loading a sample to levels that exceed the expected in situ effective stress (σ′) and allowing the pore pressure to dissipate as the sediment settles. The change in sample height under each new load is used to calculate the volumetric strain or void ratio (e) at the end of each step and defines the sediment's compressibility. Because soils are not perfectly elastic, the deformation behavior they exhibit depends on the stress history of the sample. This allows four critical parameters to be derived from a consolidation test:

1. The compression index (C_c), which defines the sediment compressibility as the slope of the e-log(σ′) curve during loading;
2. The recompression index (C_r), which is the slope of the e-log(σ) curve during unloading;
3. The preconsolidation pressure (P_c'), interpreted as the maximum past effective stress that the sediment has experienced and calculated using the curve fitting method of Casagrande (1936); and
4. The void ratio of the sediment upon deposition (e_o) (Fig. F4) (Moran et al., 1995; MacKillop et al., 1995).

F4. Hypothetical consolidation results, p. 21.

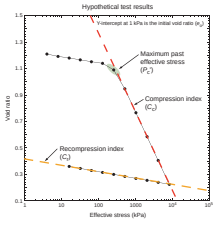

In addition to these four parameters, the time deformation behavior of the sediments can be used to determine the relationship between permeability and void ratio for the sediment.

Whole-round samples, taken shipboard from visually undisturbed sections of core, were sealed with wax, immersed in seawater, and kept refrigerated at 4°C after being shipped to the Marine Geomechanics Laboratory (University of Rhode Island). Prior to testing, the samples were removed from the sealed core liner and trimmed to a standard height of 2 cm and a diameter of 4.97 cm. Once trimmed, the wet mass of the sample was recorded before the sample was transferred into the consolidation cell that is immersed in de-aired, ultraviolet-treated seawater taken from Narragansett Bay, Rhode Island. The cell is con-

structed of stainless steel and allows sediment deformation to occur only vertically. The sample is set within the cell and placed between two porous stones. Saturated filter papers are used to separate the sample from the porous stones and prevent fine-grained sediment particles from blocking the drainage paths through the stones. After the cell is assembled, it is transferred to the consolidometer, where testing begins. General sample preparation and testing procedures followed the guidelines set out by the American Standards and Testing Materials (ASTM) standard D2435-04 (ASTM International, 2007). One-dimensional incremental load consolidation tests were conducted using one of two instruments: (1) an ELE International lever arm consolidometer or (2) a fully automated Loadtrack consolidation frame and data acquisition software system manufactured by Geocomp. Using the selected sample diameter, both systems were capable of applying loads of as much as 10 MPa.

The Geocomp assembly continuously monitors and records variations in both the applied load and sediment height. Prior to the start of each test, the loading sequence is entered into the software, with both a maximum and minimum time specified for the duration of each step. For this testing program, the Geocomp system was programmed to move to the next loading step 30 min after the end of primary consolidation. Primary consolidation is defined as the period over which the change in specimen height is associated solely with the dissipation of pore water pressure, whereas secondary consolidation is defined as strain associated with the realignment of particles within the sediment matrix (Terzaghi, 1943; Sridharan and Rao, 1982). The most reliable method for assessing the end of primary consolidation (EOP) is through the measurement of pore pressures during loading and settlement; however, the EOP can also be reliably determined by analyzing the time deformation data during settlement. No pore pressure measurements were performed during testing, and for all tests, the EOP was determined by analyzing the time deformation data using Taylor's (1948) square root of time method.

Along the virgin compression curve, where permeability measurements were acquired, secondary consolidation was allowed to progress until permeability tests were completed; typically this was ~24 hr, but in some instances where the permeability was exceptionally low, testing took between 3 and 5 days.

On the lever arm system, samples were allowed to settle for 24 hr after the application of each new load. During loading and settlement, the change in specimen height was monitored using both a dial gauge and a digital displacement transducer connected to acquisition software. Similar to the Loadtrack tests, secondary consolidation was allowed to proceed during permeability tests.

Permeability

Permeability (K) is an intrinsic property of the sediment matrix, whereas the rate of fluid flow through sediment is a function of both the intrinsic permeability and the physical properties of the flowing fluid. The rate of fluid flow is termed Darcy's coefficient of permeability, or hydraulic conductivity (k). The relationship between hydraulic conductivity and permeability is expressed by

$$K = k\rho g/\mu, \quad (1)$$

where

K = intrinsic permeability (L^2),
k = hydraulic conductivity (L/T),
ρ = pore fluid density,
g = gravitational acceleration, and
μ = fluid viscosity.

The hydraulic conductivity is reported here and normalized to seawater having a density of 1.024 g/cm^3 at 20°C.

The flow of fluids through marine sediments plays an important role in regulating the temporal and spatial evolution of petrophysical properties. Information on the relationship between void ratio and permeability for a given sediment type are used to assess the role and impact of fluid flow. Void ratio-permeability relationships are derived from consolidation tests using Terzaghi's (1943) one-dimensional consolidation theory or measured directly using a low-gradient flow-pump technique at the end of each incremental load during testing. Terzaghi's derivation of permeability is calculated using

$$k = C_v \rho g A_v/(1 + e), \quad (2)$$

where

k = hydraulic conductivity;
C_v = coefficient of consolidation, determined using either the curve fitting procedure of Taylor (1948) or Casagrande (1936) on the time deformation data during a given incremental load;
A_v = slope of the load-displacement curve; and
e = average void ratio over the incremental load for which the hydraulic conductivity is being determined.

This theoretical derivation is based upon a number of nested assumptions. It requires that the sample be homogeneous and 100% saturated. The solids and the water in pore spaces are assumed to be incompressible, with drainage occurring solely from vertical compression. It requires that effective stress maintain a unique relationship with the void ratio of the sample, which implies that both the slope of the consolidation curve (A_v) and Darcy's coefficient of permeability (hydraulic conductivity [k]) remain constant during any loading step. This condition of maintaining a unique relationship between effective stress and void ratio assumes that only primary consolidation occurs. Permeability estimates made using Terzaghi's one-dimensional theory tend to be slightly lower than actual permeability because secondary consolidation consistently plays a small role in the deformation of a sample under a load (MacKillop et al., 1995).

A more accurate way of determining hydraulic conductivity is through direct measurement using a low-gradient flow-pump technique. Recommendations for low-gradient testing of fine-grained sediments using a flexible-wall permeameter are outlined in ASTM designation D 5084-90 (ASTM International, 1990). The same testing procedures can be applied using a consolidation cell. Flow pump tests were conducted at the end of primary consolidation at each step along the virgin compression curve for selected samples. Constant rate of flow tests apply a known flow rate (q) through a sample. This flow rate establishes a head difference across the sample that is monitored using a differential pore pressure transducer. When the head equilibrates, a

steady-state gradient is established (i) and the hydraulic conductivity is calculated using Darcy's law:

$$q = kiA, \tag{3}$$

where

- q = known flow rate (L^3/T),
- k = hydraulic conductivity (L/T),
- i = dimensionless hydraulic gradient ($\Delta h/\Delta l$), and
- A = cross-sectional area of the sample (L^2).

Terzaghi's theory was used here to calculate sediment permeability during loading along the virgin compression curve for each sample. Where hydraulic conductivities were large enough for direct measurements, complementary permeability measurements were made using a low-gradient flow-pump technique. During flow pump testing, three flow rates were attempted and applied in both directions across the sample, resulting in a maximum of six direct measurements of hydraulic conductivity at each void ratio. Because Darcy's law states that the hydraulic conductivity should be independent of flow rate, the slope of a q-i plot at a given void ratio should be linear. Nonlinearity is an indication that Darcy's law has been violated and the measurements are invalid. The slope of the q-i plot was used for each series of measurements to define the hydraulic conductivity of the sample at a particular void ratio. The regression of the q-i data was forced to pass through the origin because a hydraulic gradient does not exist when the flow is zero. An e-log(k) relationship, in the form of an exponential function, is presented for each sample. When flow pump measurements existed, these were used to define the relationship and are deemed more accurate than derived measurements. In the absence of flow pump measurements, the derived permeability data were used to calculate the e-log(k) relationship for that sample.

Effective Stress

Effective stress is defined as the stress that is passed between particles in the sediment matrix and is calculated by removing the fluid pressure (u) from the lithostatic overburden, or total stress (σ):

$$\sigma' = \sigma - u. \tag{4}$$

If hydrostatic fluid pressures are assumed, σ' can be directly calculated using bulk density data:

$$\sigma' = (\rho_s - \rho_w)hg, \tag{5}$$

where

- ρ_s = sediment bulk density,
- ρ_w = density of seawater, and
- h = burial depth.

The in situ effective stress was calculated using the index property–derived bulk density values and the composite depth scales generated on

board the ship. No rebound correction was applied to the depth scales and calculations assume hydrostatic fluid pressures. The average bulk density was used to calculate the effective stress between consecutive downhole samples and rounded to the nearest 5 kPa.

Stress History

The stress history of sediments is often described using the overconsolidation ratio (OCR), which is a ratio of P_c' and the in situ σ' under hydrostatic conditions (OCR = P_c'/σ'). An OCR > 1 represents an overconsolidated sediment. Overconsolidation arises when an overburden pressure is removed from a consolidated sediment column. Such conditions arise, for example, with glacial loading and subsequent melting or lithologic loading with subsequent removal of sediment by erosion. An OCR ≅ 1 indicates that the sediment is normally consolidated, meaning the current in situ effective stress represents the maximum stress the sample has experienced. A normally consolidated state implies that hydrostatic fluid pressures are present in the sediment column. Sediments with an OCR < 1 are underconsolidated, a state which suggests the presence of excess pore pressures within the sediment column. Excess pore pressures develop through disequilibrium compaction associated with high sedimentation rates or the development of an overlying hydraulic seal, which impedes the dissipation of pore waters (Rubey and Hubbert, 1959; Fertl, 1976).

By definition, the OCR is a more sensitive indicator of stress state in near-surface sediments when compared with deeply buried formations. In shallowly buried sediments where σ' < 500 kPa, uncertainties associated with sample disturbance and effective stress calculations can have significant impacts on the calculated OCR. Because of this uncertainty, Dadey and Silva (1989) used OCR ≥ 1.2 to represent overconsolidation and OCR ≤ 0.7 for underconsolidation. As the depth of burial increases, a greater offset between P_c' and the in situ σ' is required for a significant OCR ratio to develop. Furthermore, the accuracy in the evaluation of P_c' decreases at higher effective stresses because it is determined using a curve-fitting method on a log-linear plot.

Void Ratio

During sample preparation, an ~30 g subsample was used to determine the void ratio of test specimens prior to consolidation by measuring wet and dry mass. Drying was performed at 105°C over a period of 24 hr. The salt-corrected water content was calculated from the wet and dry mass of the subsample using

$$w = (M_{wet} - M_{dry})/[M_{dry} - (0.035M_{wet})], \quad (6)$$

where

w = water content (%),
M_{wet} = wet mass of the subsample (g), and
M_{dry} = dry mass of the sample.

The calculated water content was used to determine the mass of solids and liquid within the test sample:

$$M_{solid} = M_{sample}/[1 + (w/100)] \text{ and} \quad (7)$$

$$M_{water} = M_{sample} - M_{solid}. \quad (8)$$

Using the specific gravity (G_s) of the sample, the volume of solids (V_s), water (V_w), and air (V_a) were determined:

$$V_s = M_{solid}/G_s, \quad (9)$$

$$V_w = M_{water}/1.024 \text{ g/cm}^3, \text{ and} \quad (10)$$

$$V_a = V_T - V_s - V_w, \quad (11)$$

where V_T is the total sample volume calculated from its height and diameter.

Specific gravity was either measured directly in the laboratory or derived from shipboard measurements of grain density. When derived from shipboard moisture and density data, the average grain density for the entire core was used. The void ratio of the sample is defined as

$$e = V_v/V_T, \quad (12)$$

where

$$V_v = V_a + V_w \text{ and} \quad (13)$$

$$V_T = V_a + V_s + V_w. \quad (14)$$

The calculated void ratio was used to define the void ratio of the test specimen prior to testing. For the two black shale samples (Samples 207-1257C-13R-1, 140 cm, and 207-1258B-45R-4, 45 cm), residues from oven drying at 105°C were weighed before heating to 550°C for 1 hr. This allowed the total organic carbon (TOC) content to be determined using a loss on ignition approach:

$$\%_{org} = (M_{100} - M_{550})/M_{100}, \quad (15)$$

where

$\%_{org}$ = total organic content,
M_{100} = mass of the sample after drying at 100°C,
M_{550} = mass of the sample after drying at 550°C, and

$$TOC = \%_{org} \times 0.44, \quad (16)$$

where 0.44 represents an approximate contribution of organic carbon to the molecular weight of organic material by assuming a cellulose composition.

RESULTS

Consolidation tests were performed on 12 samples from five of the major lithostratigraphic units used to describe sediments recovered during Leg 207. The deepest sample came from Site 1261 at a depth of 364

meters composite depth (mcd) and the shallowest from 26 mcd at Site 1259. A summary of consolidation results is presented in Table T1 and includes the stress history–related calculations of in situ σ′, P_c', and the OCR, as well as the sediment compressibility coefficients (C_c and C_r) and the calculated e_o.

No corrections were applied for the effects of sample disturbance. Disturbances related to coring, sampling, and preparation of the sample all result in an underestimate of P_c' and reduce both e_o and C_c. Therefore, disturbance masks the effects of overconsolidation in test specimens. A qualitative approach for evaluating sample disturbance is assessing the shape of the consolidation curve (e-log[σ′]). A sharp transition into the virgin compression curve suggests a high-quality sample. A more quantitative approach is by calculating the amount of volumetric strain that accumulates prior to reaching P_c' (Lunne et al., 1999). Developed primarily for the evaluation of samples from near-surface sediments and soils, Lunne's method evaluates sample quality using ratings between excellent and very poor. Evaluation includes consideration of the OCR, with higher levels of strain permitted for samples with low OCR values (Table T2). The majority of the samples tested here experienced between 5% and 10% strain before reaching P_c'. Using the evaluation criteria of Lunne et al. (1999), the quality of these samples range from poor to good/fair (Table T1). The relatively high degree of sample disturbance results from the depth of burial of the samples and the type of sampling tools used to collect them, in this case the rotary core barrel system. In the majority of marine sediments, there exists an order of magnitude difference in C_r and C_c (Holtz and Kovacs, 1981). At Site 1261, the high elasticity of the Neogene nannofossil clays reduced the difference between C_r and C_c, thus increasing the level of apparent sample disturbance.

Significant levels of overconsolidation, as evidenced by the calculated OCR (see Table T1), occur in samples from Sections 207-1257C-1R-2, 207-1257C-6R-3, and 207-1259A-3R-5. These results are consistent with an interpretation of mass wasting on the eastern flank of the rise based on seismic reflection data (Fig. F5) (Shipboard Scientific Party, 2004b).

An estimate of the magnitude of the erosional events is calculated by determining the amount of material required to account for the difference between P_c' and a hydrostatically determined σ′ (Table T1). The removed overburden is added to the current effective stress profile to calculate the corrected effective stress profile. Predictions of $e_{\text{in situ}}$ are made by combining the corrected effective stress profile with the compression indexes derived from consolidation tests using:

$$e_{\text{in situ}} = e_{\text{lab}} - C_r\log(\sigma'), \text{ and} \quad (17)$$

$$e_{\text{predicted}} = e_o - C_c\log(\sigma'), \quad (18)$$

where

$e_{\text{in situ}}$ = rebound-corrected laboratory measurement of void ratio and
$e_{\text{predicted}}$ = void ratio of sediments consolidating along the virgin compression curve until they reach the determined in situ effective stress.

T1. Laboratory consolidation results, p. 30.

T2. Lunne's criteria, p. 31.

F5. Seismic reflection profile of the flank of Demerara Rise, p. 22.

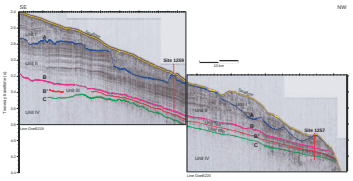

A close agreement between the predicted and measured *e* supports the stress history interpretation and permits the application of the test-derived *e*-log(*k*) relationships to determine the current in situ *k* profile.

Permeability results are summarized in Table T3 and include calculated variables (C_v and A_v) used to derive *k* from the time deformation data, as well as the calculated *k* for each set of low-gradient flow pump tests. A table is also presented summarizing q, *i,* and *k* for each set of flow pump tests (Table T4). Individual sample results from consolidation and hydraulic conductivity tests are presented in Figure F6.

One sample, Sample 207-1261A-4R-2, 80 cm, was tested using both the lever arm consolidometer and the Geocomp system. Direct measurements of *k* were performed on the lever arm system during test B. Prior to flow measurements, the sample was unloaded to 30 kPa, when a leak was detected in the consolidation cell. After the sample was reloaded and consolidation began to proceed along the virgin compression curve, *k* tests were started.

Very low permeability in a few samples either reduced the number of flow rates applied at any given *e* or, in one case, precluded the use of low-gradient flow pump measurements. A steady-state hydraulic gradient could not be established across Sample 207-1258B-36R-2, 8 cm (344.49 mcd), a Maastrichtian nannofossil chalk with forams. Flow pump tests were not possible on two other samples, Samples 207-1261A-13R-4, 140 cm, and 20R-1, 140 cm, because of leaks that developed in the consolidation cell. However, results from samples taken from this same lithostratigraphic unit at Site 1261 show excellent agreement between the derived and measured permeability determinations and suggest that the derived *k* values are correct.

The greatest offsets between the derived and measured *k* values occurred in Samples 207-1257C-1R-2, 140 cm, and 13R-1, 130 cm. In both cases, the flow pump measurements were selected as being representative of the sample's permeability. The ability to derive *k* from Terzaghi's one-dimensional theory of consolidation requires that over the analyzed period of settlement, changes in void ratio maintain a unique relationship with changes in effective stress (Holtz and Kovacs, 1981). If secondary consolidation occurs (i.e., the rearrangement of particles within the sediment), both the void ratio and permeability can change without accompanying changes in the effective stress and this assumption is no longer valid (Holtz and Kovacs, 1981). In marine sediments, permeability estimates made using Terzaghi's theory tend to be slightly lower than the actual permeability (by a factor of 2–4), with secondary consolidation consistently playing a small role in the deformation of a sample under a load (MacKillop, 1995). In organic-rich soils, secondary compression can be greater than primary consolidation during loading (Hobbs, 1986). Sample 207-1257C-13R-1, 130 cm, was a black shale with a TOC content of 8.2 wt%. Differences between the flow pump measured and derived permeability curves for this sample may be associated with a high level of secondary compression during loading. Although secondary consolidation may have been a factor in the underestimated *k* for Sample 207-1257C-1R-2, 140 cm, it should not have been as significant as in the high organic content black shale sample. Other assumptions of Terzaghi's theory that may not have been valid during the testing of Sample 207-1257C-1R-2, 140 cm, include: (1) that the sample be homogeneous and 100% saturated, (2) that the solids are incompressible, and (3) that drainage occurs from compression in one dimension (Terzaghi, 1943).

T3. Derived and measured hydraulic conductivity results, p. 32.

T4. Low-gradient flow pump results and *k* calculations, p. 33.

F6. Consolidation and permeability test results, p. 23.

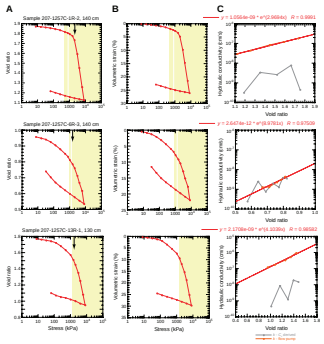

The other sample from the black shale sequences was Sample 207-1258B-45R-4, 45 cm (TOC = 6.3 wt%). During testing, a leak was discovered around the perimeter of the sample. The leak prevented the establishment of a hydraulic gradient across the sample. After unloading and sealing the leak, hydraulic conductivity measurements were conducted at 6144, 7140, and 8100 kPa. Results from flow pump tests on Sample 207-1257C-13R-1, 130 cm, are used to construct *e*-log(*k*) relationships for the black shales. Estimates from these tests give a lower hydraulic conductivity for void ratios greater than ~0.7 and higher estimates when the void ratio is less than ~0.7 when compared to the results from Sample 207-1258B-45R-4, 45 cm (Fig. **F4**). The selection of this sample as being representative of the black shales at Sites 1257, 1259, and 1261 reduced the variability in the estimates of permeability within and between sites, perhaps masking the potential for high and low permeability lenses.

Lithostratigraphic Unit III sediments on Demerara Rise generally consisted of Maastrichtian–late Paleocene nannofossil chalks and clays. These sediments exhibited the lowest porosities recovered on the rise and often showed decimeter-scale variations between chalks and clays (Shipboard Scientific Party, 2004c). Two samples were taken from this unit, Samples 207-1257C-6R-3, 140 cm, and 207-1258B-36R-2, 45 cm. Both samples exhibited significantly different compressibility and permeability behavior, with the sample from Site 1258 being less compressible and less permeable, a state that may be linked to the diagenetic history of the sample. In constructing *e* and *k* profiles for the Unit III sediments, C_c and *e*-log(*k*) from Sample 207-1257C-6R-3, 140 cm (Tables **T1, T3**), was used at Sites 1257, 1259, and 1261. However, *e*-log(*k*) relationships from Sample 207-1258B-36R-2, 45 cm, were also plotted to give a lower limit to the permeability of sediments across this unit.

DISCUSSION

Stress History and Erosion

A complex Neogene depositional history on Demerara Rise is indicated by the prevalence of nonsynchronous slump deposits and hiatuses at the five sites drilled during Leg 207 (Fig. **F2**). The limited number of samples in this study precludes a very detailed analysis of the relationships among these events but does allow inferences to be made concerning their likely timing and magnitude.

At Site 1257, the shallowest Sample 207-1257C-1R-2, 140 cm (84.9 mcd), has an OCR of 4.08, with 1510 kPa of overburden stress removed (Table **T1;** Fig. **F3**). The high OCR of the sample argues for a significant erosional event at this site. The timing of the erosional event must be associated with either the absence of Pliocene–Pleistocene material or the early Oligocene–late Miocene hiatus identified in the recovered sediments (Fig. **F2**). Generally, sedimentation rates on Demerara Rise were between 15 and 20 m/m.y. for the early and late Eocene, slowing to 8–12 m/m.y. during the early Oligocene, and then increasing substantially during the Miocene (up to 65 m/m.y. at Site 1261) (Erbacher, Mosher, Malone, et al., 2004). The absence of significant Pliocene–Pleistocene deposits from all sites visited during Leg 207 suggests that significant accumulation of these recent sediments on the outer margin flanks is untenable. Assuming a sedimentation rate of 5 m/m.y. for the Eocene–Oligocene sediments at Site 1257 (Shipboard Scientific Party,

2004b), and taking an average bulk density of 1.59 g/cm^3, the missing material represents ~270 m (**Equation 5,** p. 6) of Eocene–Oligocene chalks that would account for nearly 54 m.y. of deposition. If the estimated sedimentation rate is increased to 10 m/m.y., the duration of deposition is only 22 m.y. and approximates the length of the early Oligocene–late Miocene hiatus at Site 1257. If the eroded material is assumed to be solely Miocene equivalent deposits of nannofossil clay, with an average bulk density of 1.72 g/cm^3 (recovered at Site 1261), the missing overburden represents ~220 m of sediment (**Equation 5,** p. 6), and with a sedimentation rate of 65 m/m.y. (from Site 1261), the missing sediment accounts for only 3.5 m.y. of deposition. The amount of overburden thus requires either a prolonged period of accumulation throughout the Oligocene and early Miocene followed by a single large erosional event or a prolonged period of deposition and erosion that ended in the middle Miocene, allowing the accumulation of significant Miocene nannofossil clays during a period of 3–4 m.y. The accumulation of this material over 3.4 m.y. is consistent with the stratigraphy from Site 1261, where 270 m of nannofossil clay were deposited between 6 and 3 Ma (Shipboard Scientific Party, 2004b). Together, this evidence suggests a late Miocene age for the lost overburden at Site 1257 and implies a stable period of deposition in the late Miocene that followed a prolonged period of continued deposition and erosion lasting from the early Oligocene to middle Miocene. The prevalence of nonsynchronous Oligocene–Miocene slump deposits at Sites 1259, 1260, and 1261 fits with the interpretation of a dynamic period of deposition and erosion extending from the early Oligocene–middle Miocene (see Fig. **F2**).

OCRs from the single sample from Site 1259 and the shallow samples from Site 1261 indicate other less substantial erosional events (Fig. **F3**). At Site 1259, an OCR of 3.21 in Sample 207-1259A-3R-5, 127 cm, represents 310 kPa of lost overburden, equivalent to ~50 m of eroded nannofossil clay. An ~30-m-thick slide deposit of reworked lower Oligocene calcareous ooze rests on top of the lower Miocene calcareous ooze and chalk where Sample 207-1259A-3R-5, 127 cm, was taken (Shipboard Scientific Party, 2004a), implying that the maximum amount of eroded material was ~80 m and occurred sometime after the early Miocene.

There is no evidence for a large erosional event in the late Miocene or Pliocene–Pleistocene at Site 1261, where the only substantial Neogene deposits were recovered during Leg 207. A single underconsolidated sample was recovered from 72 mcd at Site 1261, near the top of lithostratigraphic Subunit IB, with an age range of late Miocene–middle Pliocene (Fig. **F3**). Because this interval was spot cored, a detailed age model was not developed, but shipboard results indicate that sedimentation rates between 70–140 m/m.y. are possible for the upper 70 mcd of Site 1261 (Shipboard Scientific Party, 2004c). These high rates, combined with the low permeability of the Unit II sediments (10^{-9} cm/s), may have resulted in disequilibrium compaction, a state where sediment loading exceeds the rate at which pore water can be expelled from the consolidating strata. Downhole, the OCRs of samples from Subunit IB indicate very slight overconsolidation.

OCRs at Site 1257, and to some extent in the two samples from Site 1258, tend to decrease downhole. Below the heavily overconsolidated sample from Section 207-1257C-1R-2, the OCR for Section 207-1257C-6R-3, a Paleocene-age nannofossil chalk, also indicates an overconsolidated state as would be expected when a significant overburden has been removed from a sedimentary sequence (Fig. **F3**). However, the

magnitude of lost overburden represented by the difference between P_c' and σ′ is only 1000 kPa (Table T1). Conversely, Sample 207-1257C-16R-5, 135 cm, representing the less porous Albian claystones underlying the black shales at Site 1257, had an OCR of 0.35 (underconsolidated) and a difference between P_c' and σ′ of –1750 kPa. Using the average eroded overburden (1250 kPa) from Samples 207-1257C-1R-2, 140 cm, and 6R-3, 140 cm, a modified OCR of 0.19 is determined using

$$OCR_m = P_c'/(\sigma' + \sigma'_{\text{eroded material}}). \quad (19)$$

The largely underconsolidated nature of this sample implies that normal consolidation processes have been inhibited and that excess pore pressure is present below the black shales at this site. Although the black shale sample from Site 1257 had an OCR of 1.39, the modified OCR (Equation 19) for this sample is actually 0.72 and implies that the black shale sequence at this site was moderately underconsolidated at the time of maximum loading, which, given the arguments for the timing of the erosional event, would have been in the late Miocene. It is difficult to reconcile the highly underconsolidated sample from beneath the black shales at Site 1257 with the almost normally consolidated black shale sample. Part of the difference may be accounted for by sample disturbance, which may have reduced the P_c' estimate for Sample 207-1257C-16R-5, 135 cm. Alternatively, the black shale sample may be more normally consolidated because of the higher permeability, which allows flow channeling toward the outcrops on the margin flanks, while the lower permeability underlying Albian claystones remain overpressured. In spite of the mechanism for the drop in the OCR beneath the black shales at Site 1257, a downhole decrease in the OCR at Site 1257 is recognized, with highly overconsolidated near-surface sediments giving way to underconsolidated sediments at the bottom of the hole (Fig. F3).

Sample 207-1258B-45R-4, 45 cm, the second Cretaceous black shale sample tested, was underconsolidated with an OCR of 0.39 (Fig. F3). Unlike Site 1257, where evidence for significant erosion was found, the Maastrichtian–early Paleocene chalk from above the black shales at Site 1258 appears to be normally consolidated (OCR = 1.07). The low OCR (0.39) for the black shale from Site 1258 indicates that fluid pressures in excess of hydrostatic are present. The difference in the current in situ effective stress and the P_c' from this sample gives a rough estimate of the present excess pore pressure of 1990 kPa (Table T1).

Permeability and Fluid Flow

Permeability profiles for Sites 1257, 1259, and 1261 were constructed using the best estimates of effective stress profiles to predict the in situ void ratio profiles and applying the laboratory derived *e*-log(*k*) relationships to these profiles (Figs. F7, F8, F9). Differences in the predicted and measured void ratio profiles translate into uncertainties in the permeability profiles. These differences likely arise from variability in downhole and intersite sediment composition or the degree of diagenesis but may also include variability in stress history that cannot be identified without a more detailed sampling program. At Site 1261, this uncertainty would include the thickness of material removed during the debris flow of Subunit IC, which represents a gap of ~30 m.y. in the sediment record (Fig. F3).

F7. Site 1257 effective stress, void ratio, and hydraulic conductivity profile, p. 27.

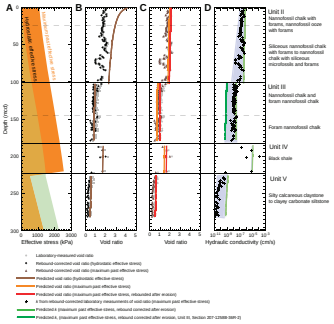

F8. Site 1259 effective stress, void ratio, and hydraulic conductivity profile, p. 28.

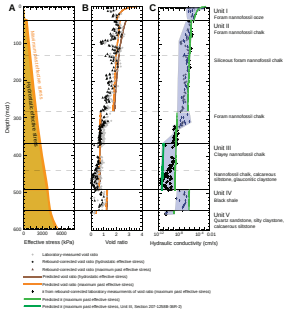

F9. Site 1261 effective stress, void ratio, and hydraulic conductivity profile, p. 29.

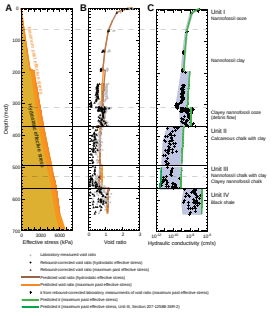

The general observation that underconsolidation increases with depth at all the studied sites suggests that fluid pressures increase above hydrostatic toward the black shales. On the flank of Demerara Rise, the black shales at Site 1257 are currently normally consolidated to overconsolidated, but significant overpressuring exists in the underlying Albian claystones. At the time of maximum loading, the black shales at Site 1257 would have been slightly underconsolidated, as inferred from the OCR_m for Sample 207-1257-13R-1, 130 cm (Table T1). The only other sample from the black shales (taken from Site 1258) was highly underconsolidated. Although these very different stress histories may simply highlight the natural variability between and within sites on the Demarara Rise, they may also suggest that as one moves away from the steeper eastern flank, where the black shales outcrop on the outer margin, fluid pressures increase. In this scenario, the hydrostatic pressures in the black shales along the eastern flank of the rise are being maintained by lateral fluid expulsion into the water column.

Composite permeability profiles from Sites 1257, 1259, and 1261 indicate that the Cretaceous shale deposits are between 3 and 5 orders of magnitude more permeable than the Maastrichtian–Paleocene chalks and clays that overly them (Figs. F7, F8, F9). The existence of a hydraulic seal, associated with the deposition or diagenetic alteration of the low-permeability Paleocene chalks and clays, is a possible mechanism for generating the underconsolidation of the black shales and older underlying sediments. With a hydraulic seal in place, continued microbial generation of methane (Meyers et al., 2004), compaction-related dewatering, or connections to deeper-sourced fluid reservoirs and the presence of an active flow regime could all prevent normal consolidation of the black shales and underlying sediments.

Similar to the permeability structure of other passive margins, such as the New Jersey margin (Dugan and Flemings, 2000), the architecture of the Demerara Rise appears to support a large horizontal component to fluid flow. The black shale deposits serve as a high-permeability, laterally continuous conduit. Increasing sediment thickness toward the center of the rise provides a gradient in overburden to drive flow. The presence of an active flow regime within the black shales may partially explain geochemical evidence for hypersaline pore fluid in the Cretaceous shale deposits at three of the five sites (Sites 1257, 1259, and 1261) (Erbacher, Mosher, Malone, et al., 2004). A reduction in chlorinity concentrations beneath the shale sequence at Site 1257 indicates that the profiles are not the result of a diffusion gradient driven by a chloride source in the underlying synrifted sediments (Shipboard Scientific Party, 2004a).

The complex stress history of sediments on Demerara Rise makes it difficult to tie regional evidence for large-scale slope instability to elevated fluid pressures in the sedimentary column. If the Maastrichtian–Paleocene chalks and clays are acting as a hydraulic seal, then depending on the efficiency of this seal, fluid pressures would rise within the underlying black shales. Overpressure would build and either exceed the overburden pressures making the formation unstable or drive a large horizontal flow regime. These fluids would likely be focused toward the sea surface along existing faults or through the high-permeability black shales toward outcrops located on the flanks of Demerara Rise. Ongoing microbial degeneration of organic matter within the black shales (Meyers et al., 2004) would contribute to the development of overpressures and generate methane-enriched pore fluids that would migrate laterally along aquifers or vent on the margin flanks.

SUMMARY

Stress history results derived from one-dimensional incremental load consolidation tests on sediments from ODP Leg 207 are used to constrain the timing and magnitude of erosional events on Demerara Rise. These results indicate that significant sediment accumulation and subsequent erosion occurred in the late Miocene, following a prolonged period of dynamic deposition and erosion that existed between the early Oligocene and middle Miocene. OCRs tend to decrease downhole, indicating that elevated pore pressures exist in the vicinity of Cretaceous black shale deposits. The magnitude of the excess pore pressure varies across the rise, potentially increasing away from regions where the black shales outcrop on the steep margin flanks. Permeability profiles document a sharp decrease across the Maastrichtian–Paleocene chalks and clays that overly the black shales. These low permeability sediments may act as a hydraulic seal, providing a mechanism for generating excess pore pressures in Cretaceous sediments. Together with lateral variations in overburden, the permeability profiles provide the architecture for a significant two-dimensional flow regime, with the black shales acting as a laterally continuous permeable conduit. This flow regime may be able to explain anomalous pore water profiles observed in the black shales.

ACKNOWLEDGMENTS

This research used samples and/or data provided by the Ocean Drilling Program (ODP). ODP is sponsored by the U.S. National Science Foundation (NSF) and participating countries under management of Joint Oceanographic Institutions (JOI), Inc. We would like to thank JOI for funding for this research via the U.S. Science Support Program. The authors also thank Kevin MacKillop, Kevin Brown, and one anonymous reviewer who provided important suggestions to this manuscript.

REFERENCES

ASTM International, 1990. Standard test method for measurement of hydraulic conductivity of saturated porous materials using a flexible wall permeameter (Standard D5084–70). In *Annual Book of ASTM Standards:* Philadelphia (Am. Soc. Testing and Mater.), 63–70.

ASTM International, 2007. Standard test methods for one-dimensional consolidation properties of soils using incremental loading (Standard D2435-04). In *Annual Book of ASTM Standards* (Vol. 04.08): *Soil and Rock* (I): West Conshohocken, PA (Am. Soc. Testing and Mater.).

Casagrande, A., 1936. The determination of pre-consolidation load and its practical significance. *In* Casagrande, A., Rutledge, P.C., and Watson, J.D. (Eds.), *Proc. 1st Int. Conf. Soil Mech. Found. Eng.,* Am. Soc. Civ. Eng., 3:60–64.

Dadey, K.A., and Silva, A.J., 1989. Consolidation and strength of Pliocene–Pleistocene sediments from Sites 646 and 647, ODP Leg 105. *In* Srivastava, S.P., Arthur, M.A., Clement, B., et al., *Proc. ODP, Sci. Results,* 105: College Station, TX (Ocean Drilling Program), 791–796. **doi:10.2973/odp.proc.sr.105.145.1989**

Dugan, B., and Flemings, P.B., 2000. Overpressure and fluid flow in the New Jersey continental slope: implications for slope failure and cold seeps. *Science,* 289(5477):288–291. **doi:10.1126/science.289.5477.288**

Erbacher, J., Mosher, D.C., Malone, M.J., et al., 2004. *Proc. ODP, Init. Repts.,* 207: College Station, TX (Ocean Drilling Program). **doi:10.2973/odp.proc.ir.207.2004**

Fertl, W.H., 1976. *Abnormal Formation Pressures: Implications to Exploration, Drilling, and Production of Oil and Gas Resources:* Amsterdam (Elsevier).

Ge, S., Bekins, B., Bredehoeft, J., Brown, K., Davis, E., Gorelick, S., Henry, P., Kooi, H., Moench, A., Ruppel, C., Sauter, M., Screaton, E., Swart, P., Tokunaga, T., Voss, C., and Whitaker, F., 2002. Hydrogeology program planning group final report. *JOIDES J.,* 28(2):24–29.

Hart, B.S., Flemings, P.B., and Deshpande, A., 1995. Porosity and pressure: role of compaction disequilibrium in the development of geopressures in a Gulf Coast Pleistocene basin. *Geology,* 23(1):45–48. **doi:10.1130/0091-7613(1995)023<0045:PAPROC>2.3.CO;2**

Henry, P., Lallemant, S., Nakamura, K., Tsunogai, U., Mazzotti, S., and Kobayashi, K., 2002. Surface expression of fluid venting at the toe of the Nankai wedge and implications for flow paths. *Mar. Geol.,* 187(1–2):119–143. **doi:10.1016/S0025-3227(02)00262-1**

Hobbs, N.B., 1986. Mire morphology and the properties and behavior of some British and foreign peats. *J. Eng. Geol. Hydrogeol.,* 19:7–80.

Holtz, R.D., and Kovacs, W.D., 1981. *An Introduction to Geotechnical Engineering:* Englewood Cliffs, NJ (Prentice-Hall).

Lunne, T., Berre, T., and Strandvik, S., 1999. Sample disturbance effects in soft low plastic Norwegian clay. *Publ.—Nor. Geotek. Inst.,* 204:81–102.

MacKillop, A.K., Moran, K., Jarrett, K., Farrell, J., and Murray, D., 1995. Consolidation properties of equatorial Pacific Ocean sediments and their relationship to stress history and offsets in the Leg 138 composite depth sections. *In* Pisias, N.G., Mayer, L.A., Janecek, T.R., Palmer-Julson, A., and van Andel, T.H. (Eds.), *Proc. ODP, Sci. Results,* 138: College Station, TX (Ocean Drilling Program), 357–369. **doi:10.2973/odp.proc.sr.138.118.1995**

Meyers, P.A., Forster, A., Sturt, H., and Shipboard Scientific Party, 2004. Microbial gases in black shale sequences on the Demerara Rise. *In* Erbacher, J., Mosher, D.C., Malone, M.J., et al., *Proc. ODP, Init. Repts.,* 207: College Station, TX (Ocean Drilling Program), 1–18. **doi:10.2973/odp.proc.ir.207.109.2004**

Moran, K., Gray, W.G.D., and Jarrett, C.A., 1995. Permeability and stress history of sediment from the Cascadia margin. *In* Carson, B., Westbrook, G.K., Musgrave,

R.J., and Suess, E. (Eds.), *Proc. ODP, Sci. Results,* 146 (Pt. 1): College Station, TX (Ocean Drilling Program), 275–280. doi:10.2973/odp.proc.sr.146-1.225.1995

Sridharan, A., and Rao, A.S., 1982. Mechanisms controlling the secondary compression of clays. *Geotechnique,* 32:249–260.

Taylor, D.W., 1948. *Fundamentals of Soil Mechanics:* New York (John Wiley).

Terzaghi, K., 1943. *Theoretical Soil Mechanics:* New York (John Wiley).

Rubey, W.W., and Hubbert, M.K., 1959. Role of fluid pressure in mechanics of overthrust faulting, Part 2. Overthrust belt in geosynclinal area of western Wyoming in light of fluid-pressure hypothesis. *Geol. Soc. Am. Bull.,* 70:167–205.

Shipboard Scientific Party, 2004a. Site 1257. *In* Erbacher, J., Mosher, D.C., Malone, M.J., et al., *Proc. ODP, Init. Repts.,* 207: College Station, TX (Ocean Drilling Program), 1–111. doi:10.2973/odp.proc.ir.207.104.2004

Shipboard Scientific Party, 2004b. Site 1259. *In* Erbacher, J., Mosher, D.C., Malone, M.J., et al., *Proc. ODP, Init. Repts.,* 207: College Station, TX (Ocean Drilling Program), 1–110. doi:10.2973/odp.proc.ir.207.106.2004

Shipboard Scientific Party, 2004c. Site 1261. *In* Erbacher, J., Mosher, D.C., Malone, M.J., et al., *Proc. ODP, Init. Repts.,* 207: College Station, TX (Ocean Drilling Program), 1–103. doi:10.2973/odp.proc.ir.207.108.2004

Figure F1. Site map for Ocean Drilling Program (ODP) Leg 207 (figure adapted from Shipboard Scientific Party, 2004b). DSDP = Deep Sea Drilling Project.

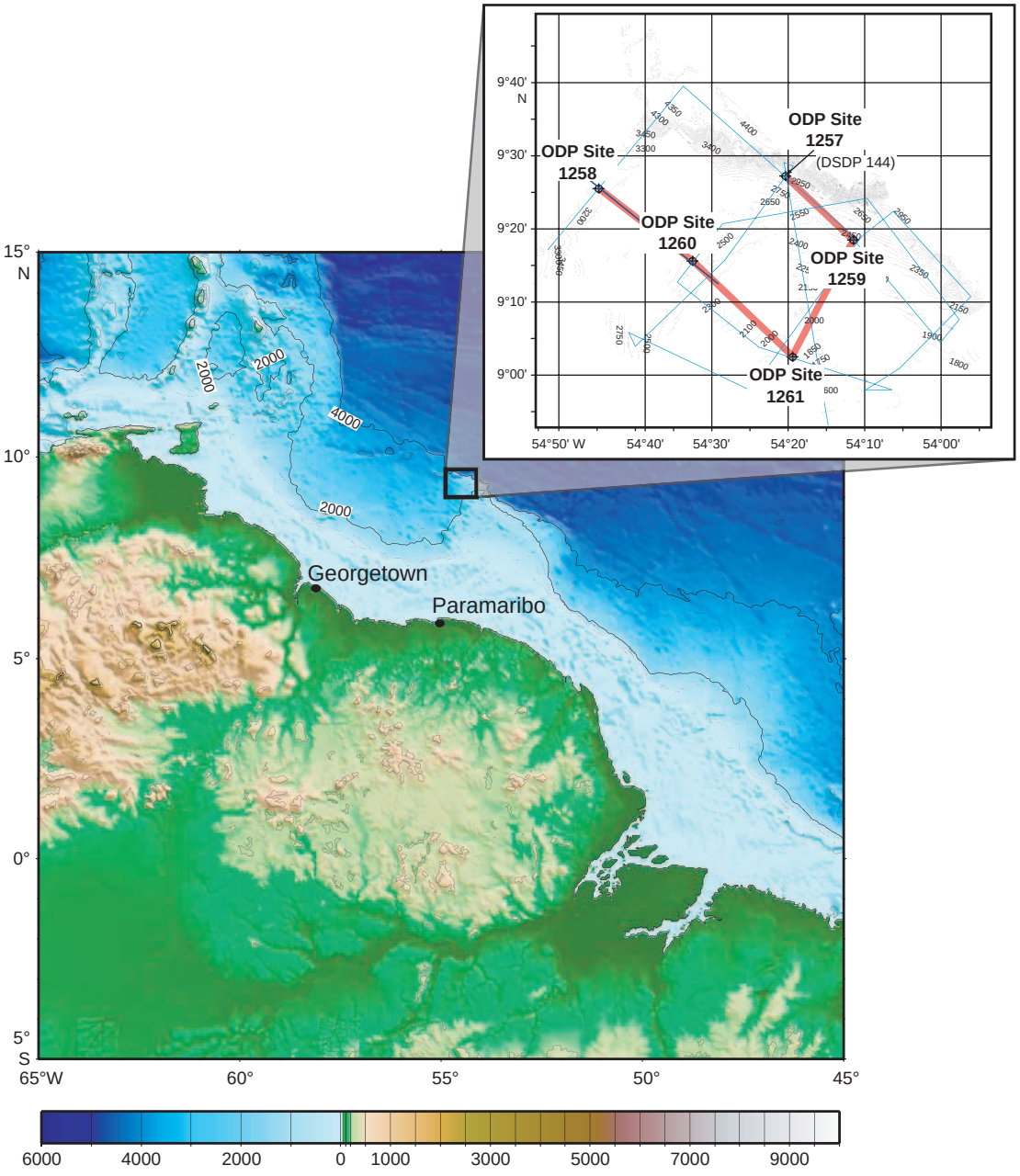

Figure F2. Schematic illustration of age and sediment type recovered from the five sites on Demerara Rise during ODP Leg 207. Recovered sediments were described using five lithostratigraphic units.

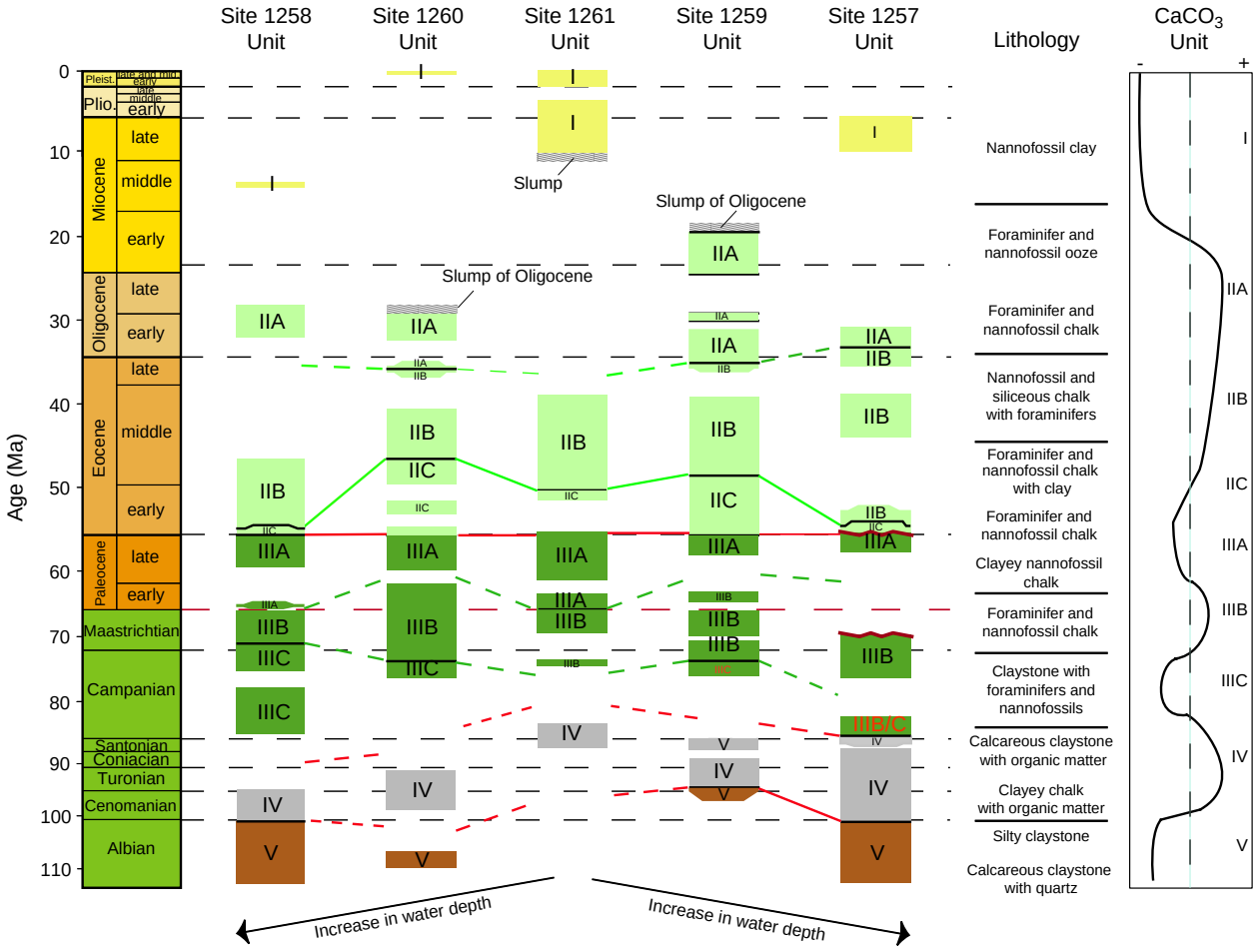

Figure F3. Location and overconsolidation ratio (OCR) of samples used in this study. Sample locations are denoted by a black box, with the OCR value offset to the left (OCR from Table T1, p. 30). Downhole velocity and porosity profiles are also presented. Velocity measurements are uncorrected for in situ temperature and pressure. Colors (blue, red, and green) indicate measurements from Holes A, B, and C, respectively. Discrete measurements of porosity (open circles) are shown alongside downhole wireline porosity logs. Stratigraphic boundaries corresponding to regional seismic markers B, B′, and C are indicated with dotted lines (see Fig. F5, p. 22, for description of seismic markers). Figure adapted from Shipboard Scientific Party (2004b). mbsl = meters below sea level.

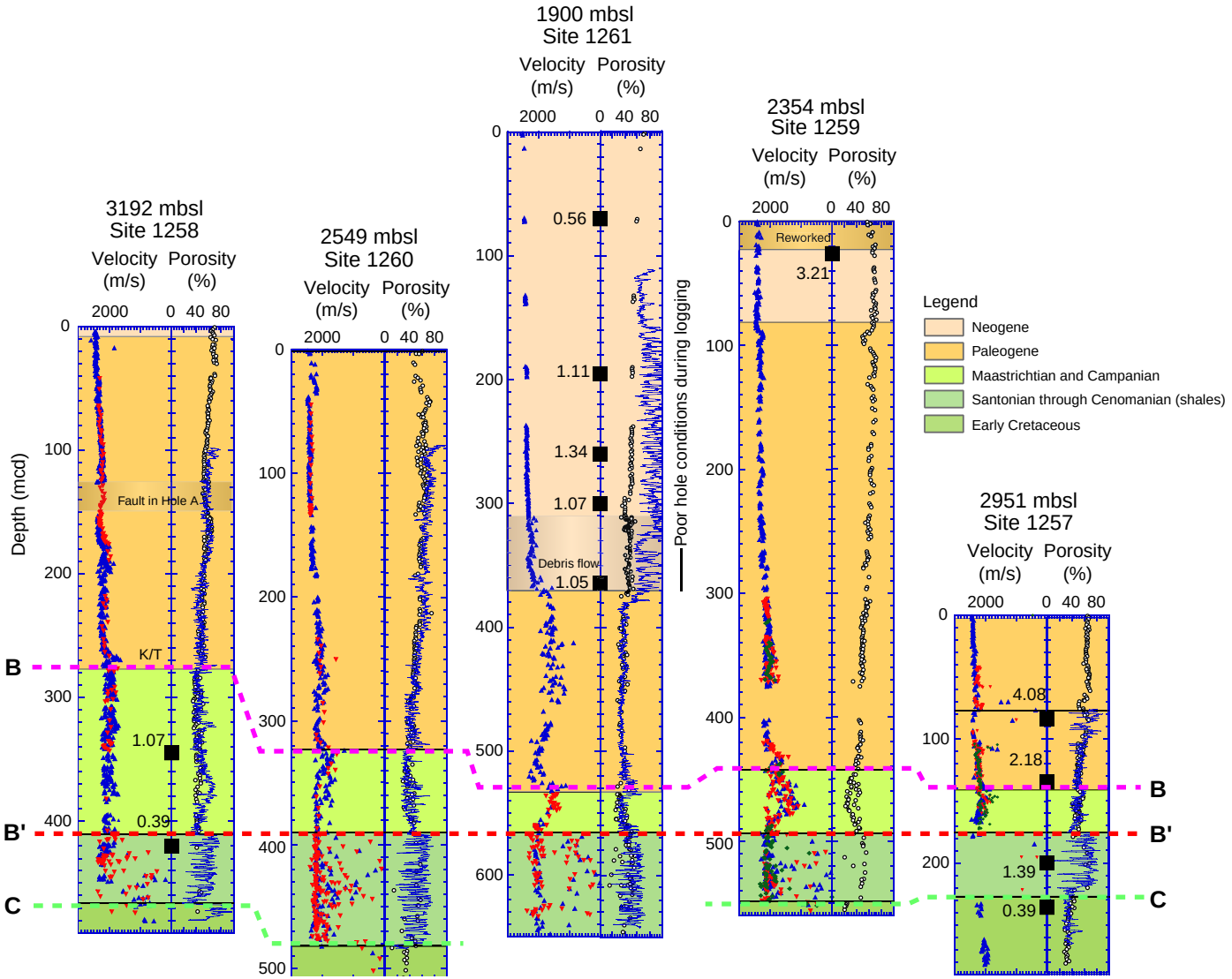

Figure F4. Hypothetical consolidation results illustrating how e_o, P_c', C_c, and C_r are determined. Void ratio is calculated by the change in sediment height that occurs as a result of primary consolidation during the course of each loading step.

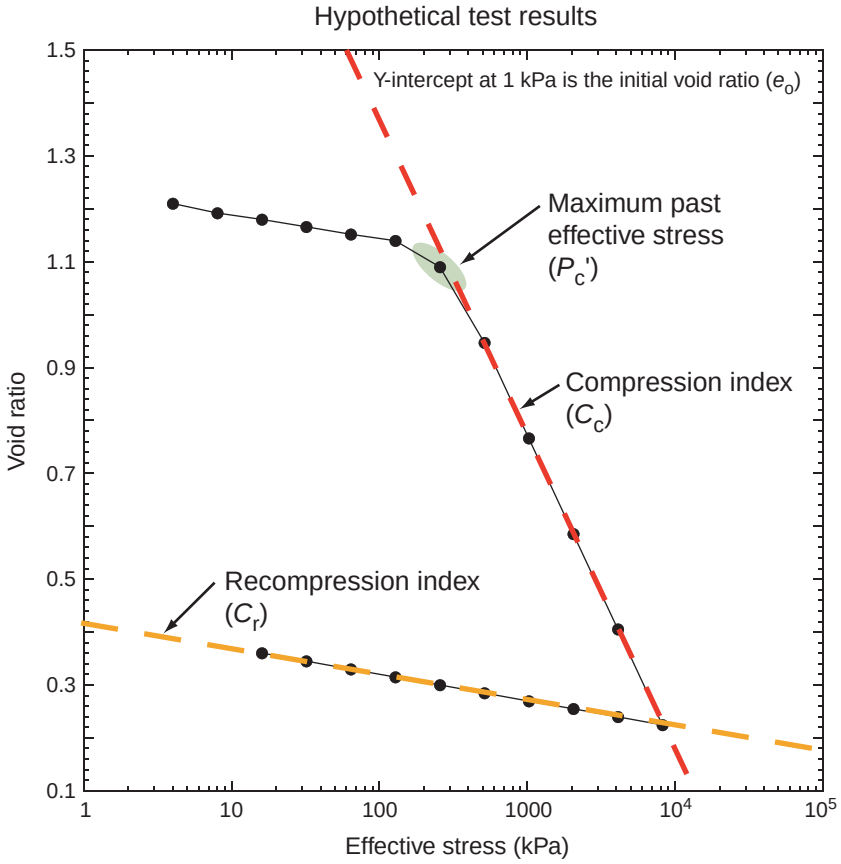

Figure F5. Seismic reflection profile of the flank of Demerara Rise showing major sedimentary units and a heavily eroded Unit I. Key regional seismic markers are illustrated with Horizon C marking the transition from synrift deposition to hemipelagic and pelagic deposition of Cretaceous black shales. Horizon B´ correlates with the top of the Cretaceous black shale sequence, and Horizon B marks the K/T boundary. Horizon A is associated with an early Miocene erosional unconformity that removed most of the Neogene sediments from the flanks of the Demerara Rise (from Erbacher, Mosher, Malone, et al., 2004).

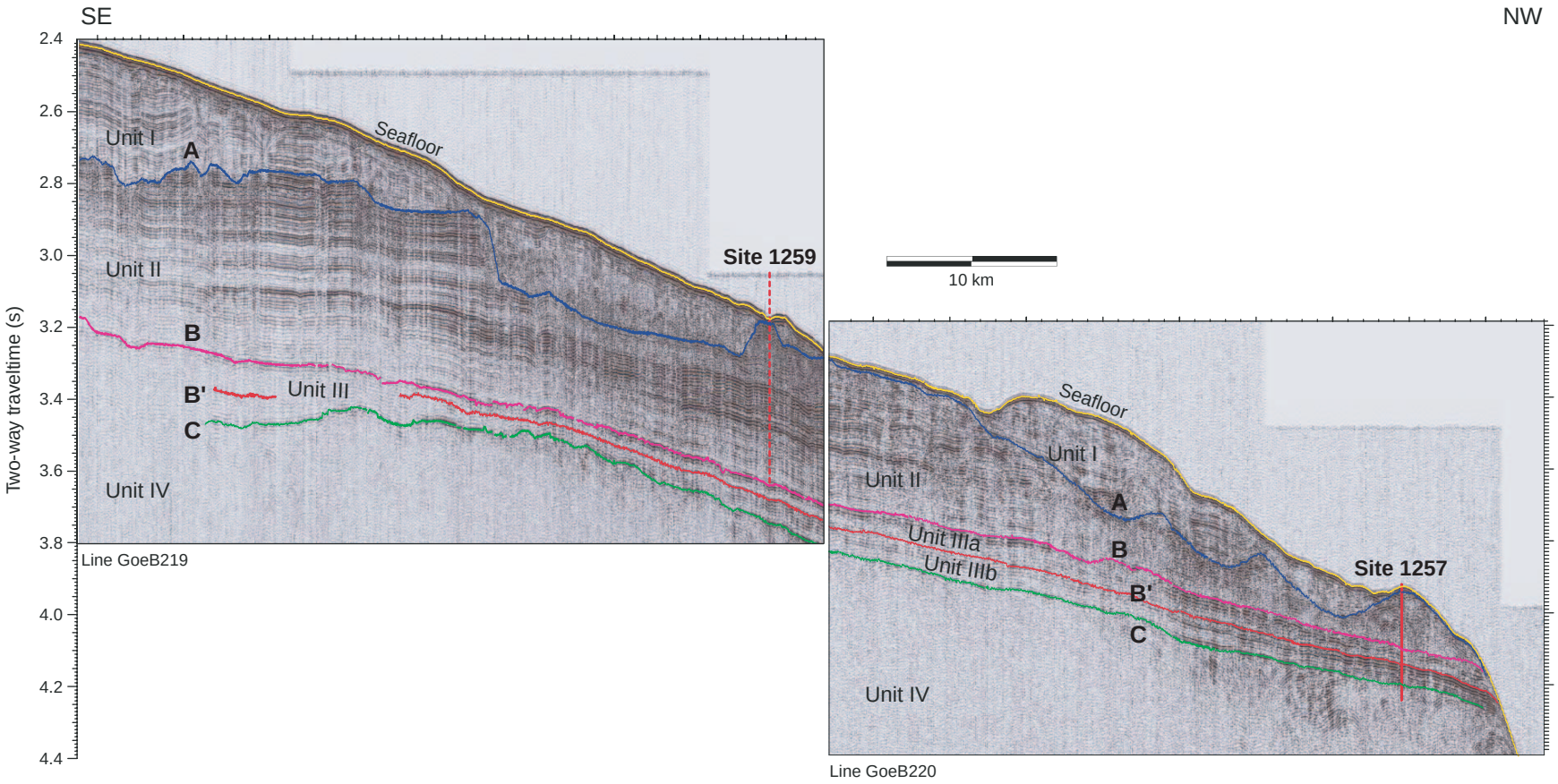

Figure F6. Results from consolidation and permeability tests presented by sample. **A.** *e*-log(σ′) curves from consolidation tests with the calculated P_c' identified by a black arrow. Shading represents the region that exceeds the calculated in situ effective stress and corresponds to stresses over which a normally consolidated sample should be proceeding along the virgin compression curve. **B.** Volumetric strain-log(σ′). The amount of volumetric strain required to reach P_c' offers a simple way to evaluate sample quality (Lunne et al., 1999). **C.** Results from low-gradient flow pump *k* tests and *k* derived from time deformation data acquired during consolidation tests. An exponential fit representing the *e*-log(*k*) relationship is displayed for each sample; red = measured *k*, blue = *k* from C_v during consolidation test. (Continued on next three pages.)

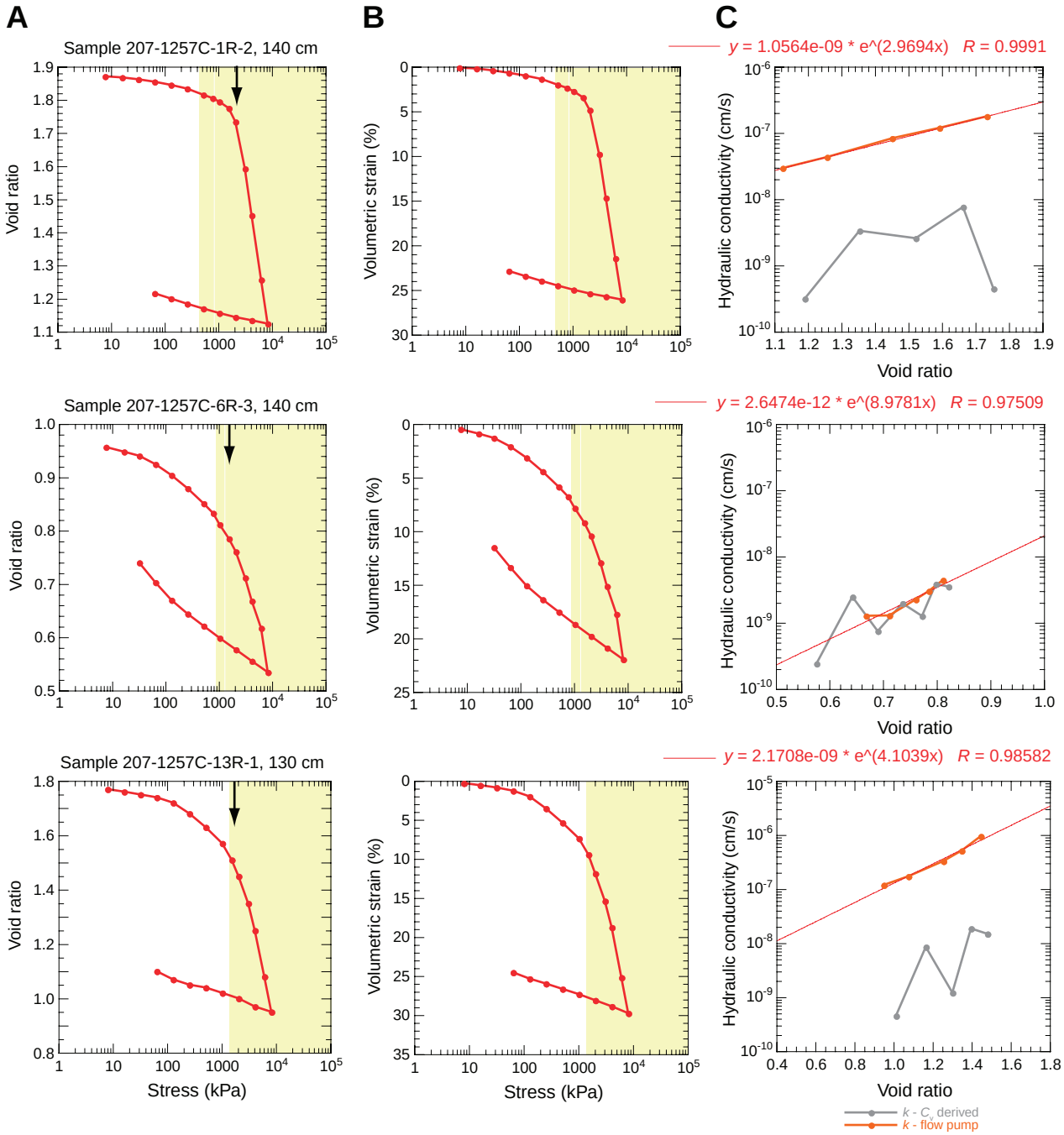

Figure F6 (continued).

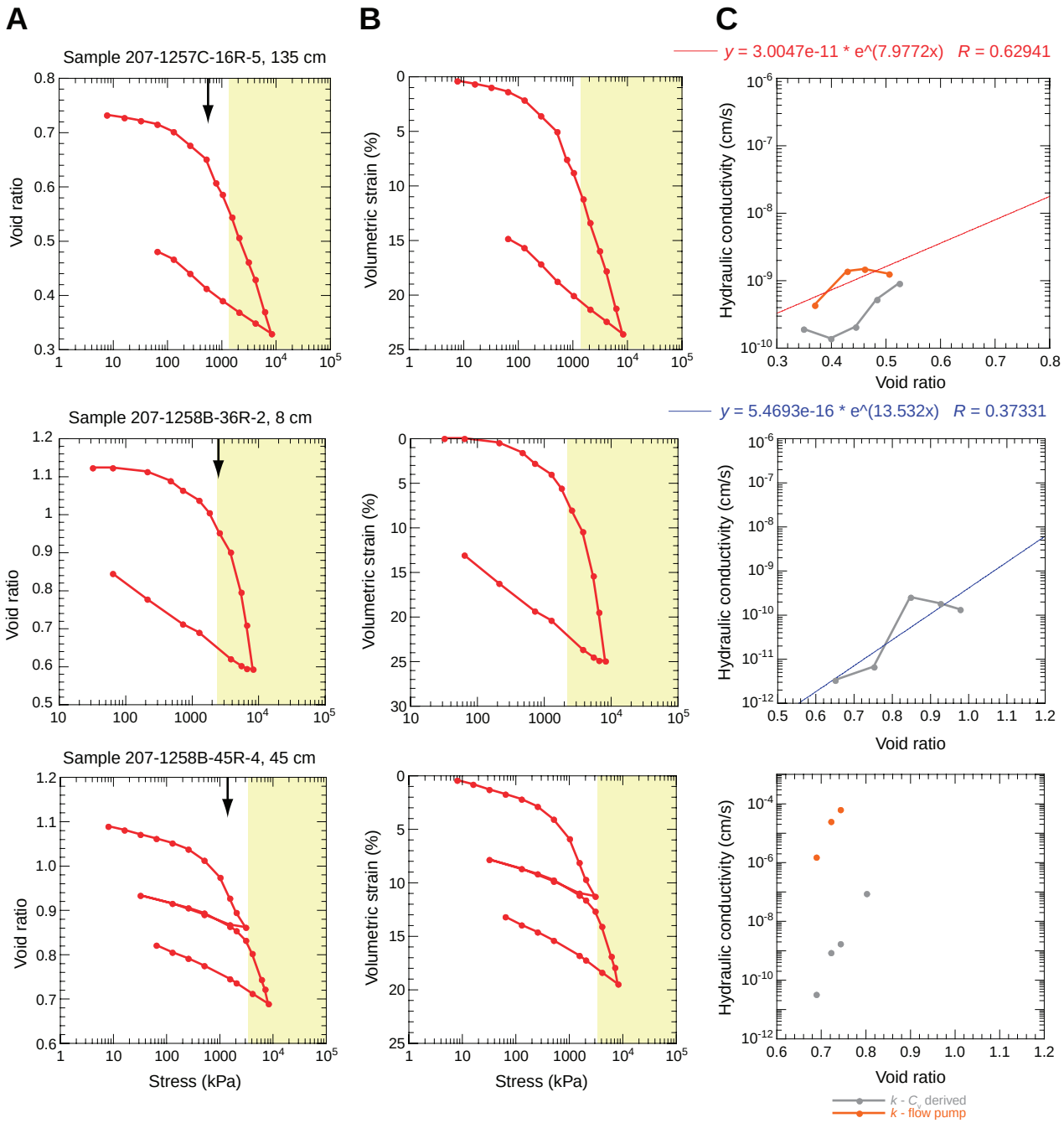

Figure F6 (continued).

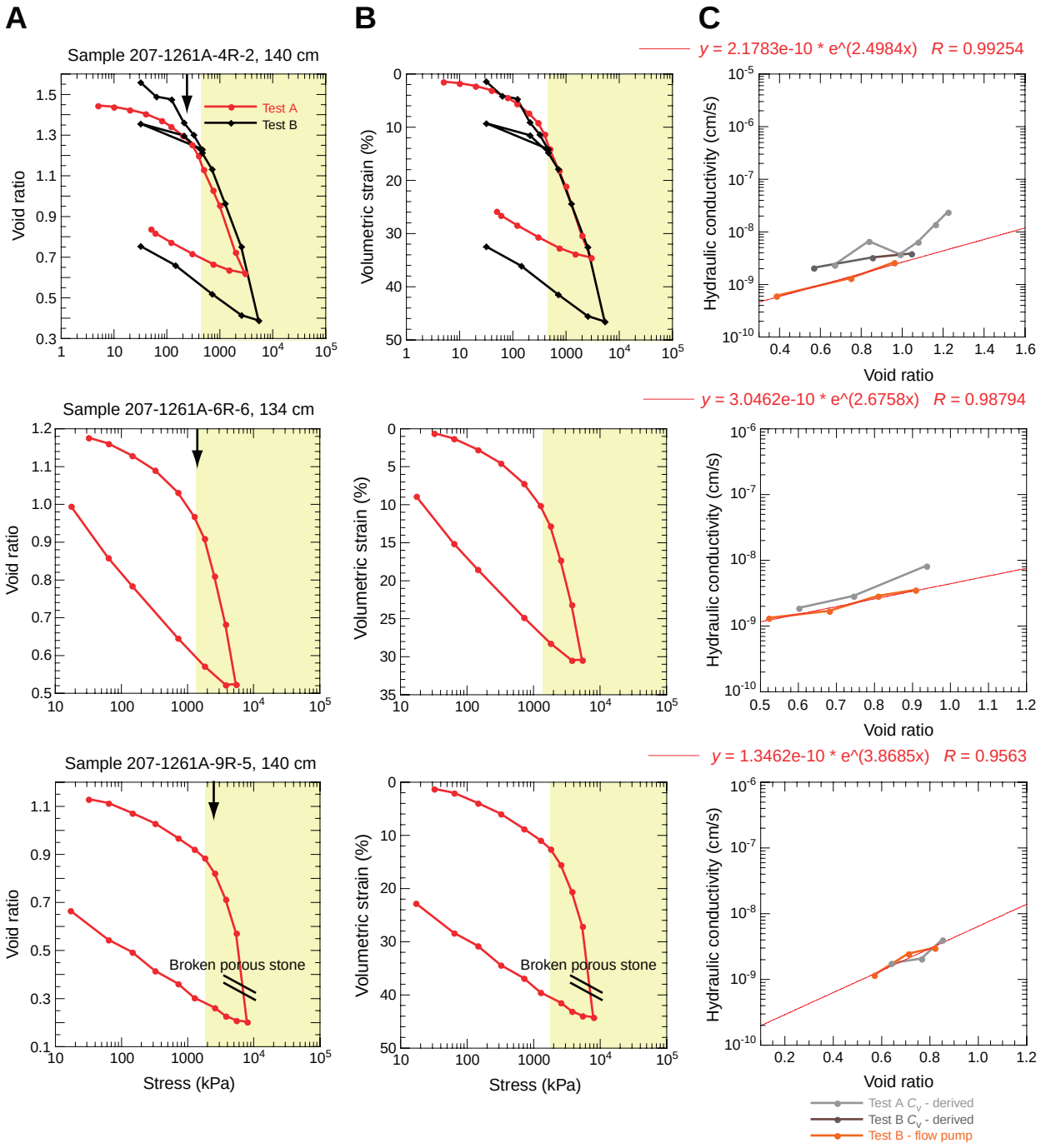

Figure F6 (continued).

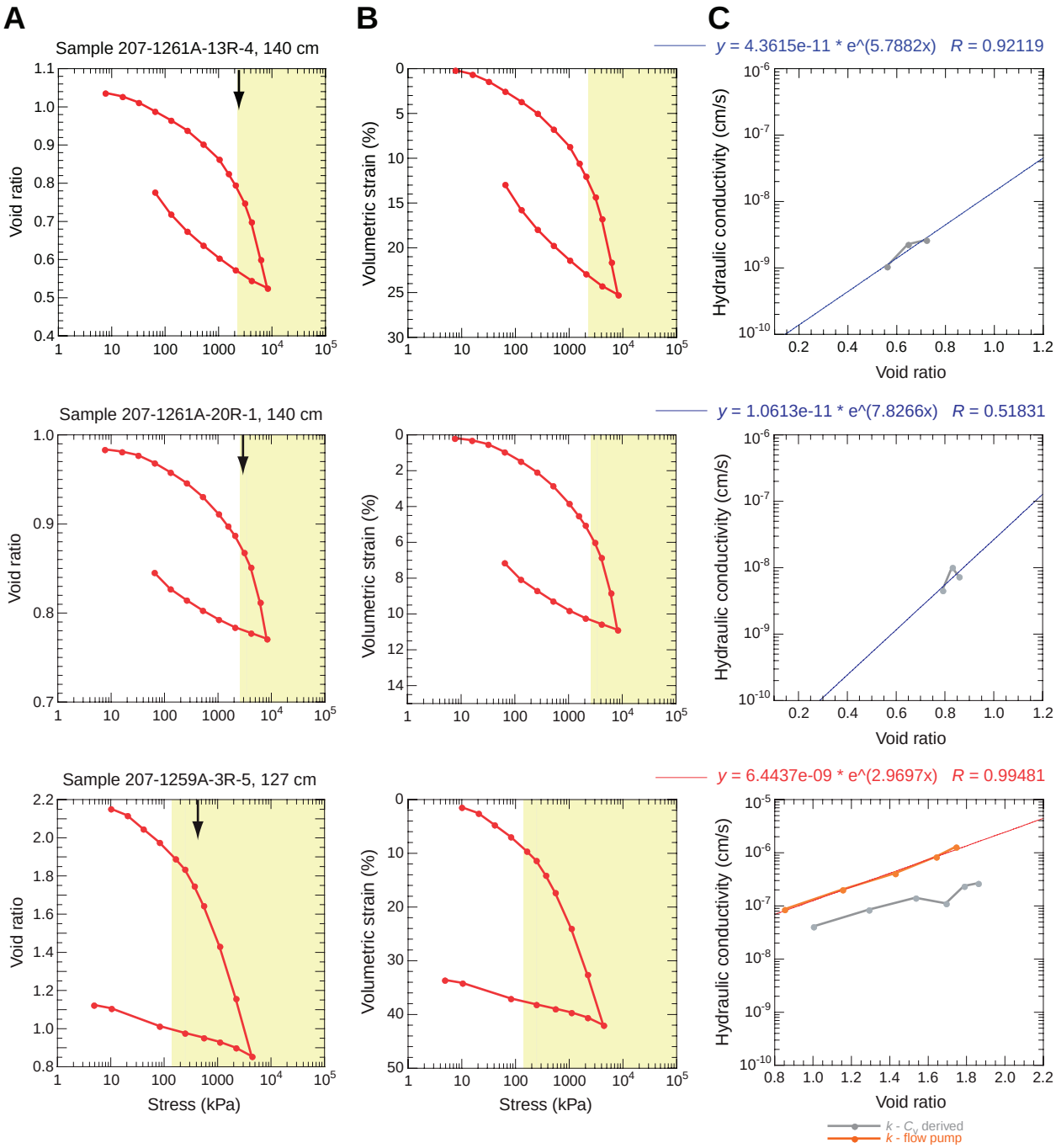

Figure F7. Effective stress, void ratio, and hydraulic conductivity profile for Site 1257. Stress history data were used to calculate the maximum past effective stress profile for the sedimentary column (**Equation 19,** p. 13) and predict in situ *e* from consolidation test results (**Equation 18,** p. 9). At Site 1257, 1200 kPa of overburden was added to the hydrostatic effective stress profile to determine the maximum past effective stress (Table **T1,** p. 30). Laboratory measurements of *e* (gray diamonds) were rebound corrected (**Equation 17,** p. 9, black triangles) using the hydrostatically determined effective stress profile (**Equation 5,** p. 6), except for Unit V of Site 1257, where significant underconsolidation was present. For this unit, the present effective stress is equal to the maximum past effective stress and is used for both rebound corrections of laboratory measurements and *e* predictions from consolidation test results. The hydraulic conductivity of sediments was calculated in two ways: (1) by using the *e*-log(*k*) relationship for individual lithotypes on the rebound-corrected laboratory measurements of *e* (black stars) and (2) by applying the *e*-log(*k*) relationship to the predicted *e* profile (orange line) (Table **T3,** p. 32). Often the predicted *e* overestimates the in situ *e*, and thus serves as an upper bound to sediment permeability. For Unit III, an upper and lower permeability were determined by applying the *e*-log(*k*) relationship from Samples 207-1257C-6R-3, 140 cm, and 207-1258B-36R-2, 45 cm. Blue shading represents a qualitative estimate for the possible range of hydraulic conductivity within each lithologic unit.

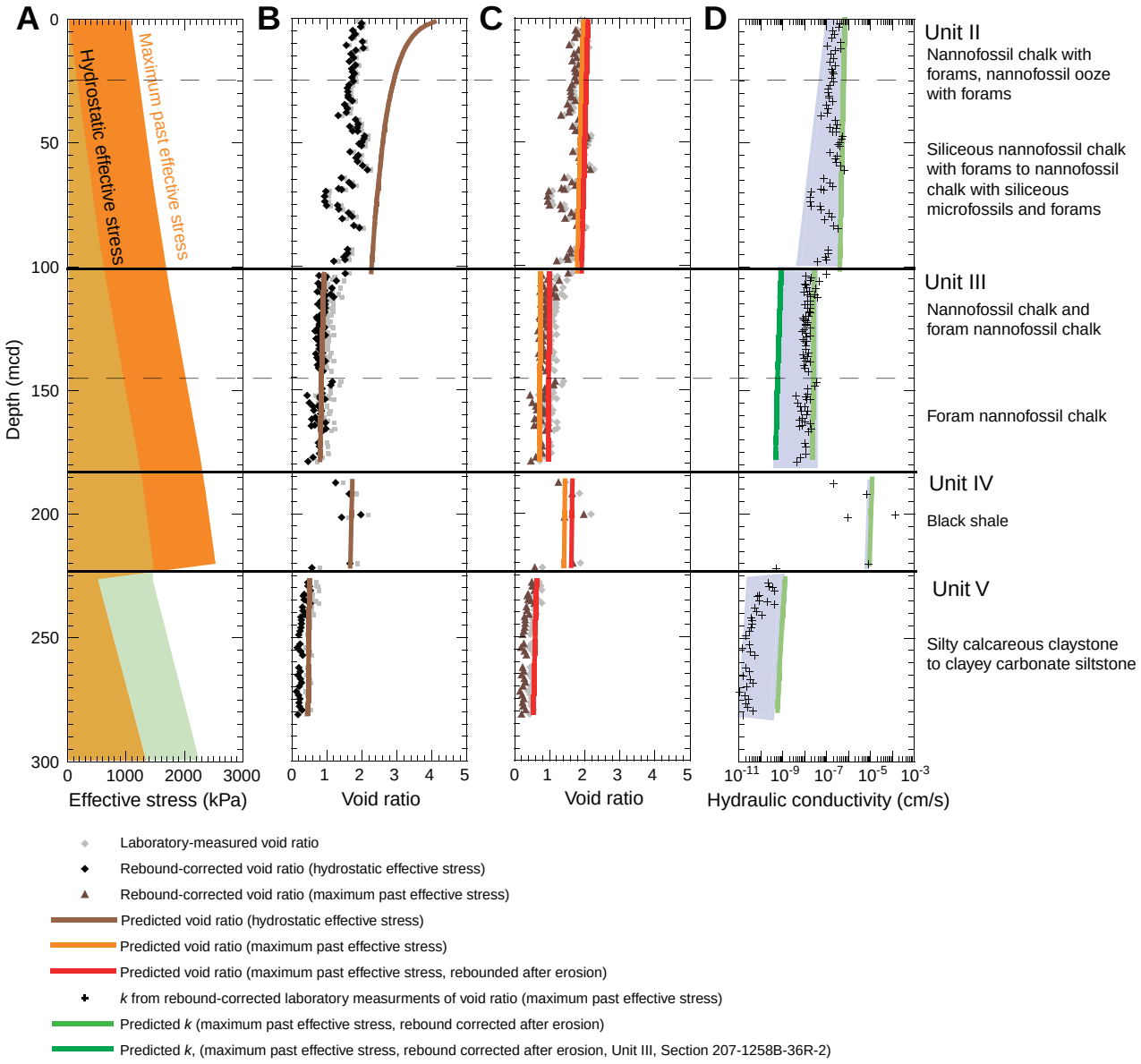

Figure F8. Effective stress, void ratio, and hydraulic conductivity profile for Site 1259. Stress history data from a near-surface Oligocene sample was used to determine the maximum past effective stress profile for the sedimentary column (**Equation 19,** p. 13) and predict the in situ *e* from consolidation test results (**Equation 18,** p. 9). At Site 1259, 300 kPa was added to the hydrostatic effective stress to predict the *e* of sediments using consolidation test results from sampled lithologic units at other sites (Table **T1,** p. 30). Laboratory measurements of *e* (gray diamonds) were rebound corrected (**Equation 17,** p. 9, black triangles) using the hydrostatically determined effective stress profile (**Equation 5,** p. 6). The hydraulic conductivity of sediments was calculated in two ways: (1) by using the *e*-log(*k*) relationship for individual lithotypes on the rebound-corrected laboratory measurements of *e* (black stars) and (2) by applying the *e*-log(*k*) relationship to the predicted *e* profile (orange line) (Table **T3,** p. 32). Often the predicted *e* overestimates the measured *e*, and thus serves as an upper bound to sediment permeability. For Unit III, an upper and lower permeability were determined by applying the *e*-log(*k*) relationship from Samples 207-1257C-6R-3, 140 cm, and 207-1258B-36R-2, 45 cm. Blue shading represents a qualitative estimate for the possible range of hydraulic conductivity within each lithologic unit.

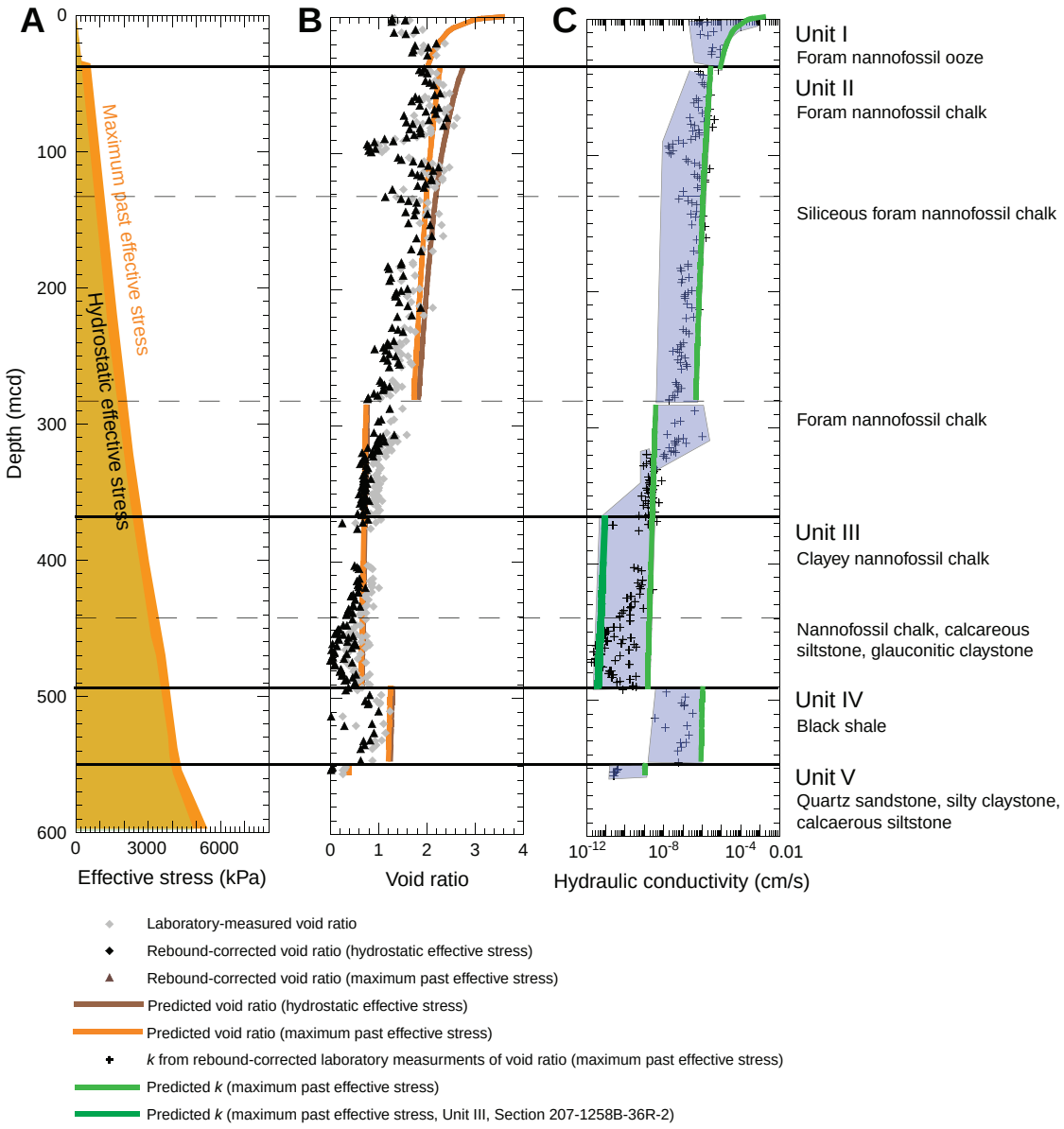

Figure F9. Effective stress, void ratio, and hydraulic conductivity profile for Site 1261. Stress history data from Unit I sediments were used to determine the maximum past effective stress profile for the sedimentary column (**Equation 19,** p. 13) and predict the in situ *e* from consolidation tests (**Equation 18,** p. 9). At Site 1261, 600 kPa (determined from the highest OCR of Unit I samples from the site) was added to the hydrostatic effective stress to predict the *e* of sediments using consolidation tests (Table **T1,** p. 30). Below Unit I, consolidation results from lithologic units recovered at other sites were used to predict in situ *e*. Laboratory measurements of *e* (gray diamonds) were rebound corrected (**Equation 17,** p. 9, black triangles) using the hydrostatically determined effective stress profile (**Equation 5,** p. 6). The hydraulic conductivity of sediments was calculated in two ways: (1) by using the *e*-log(*k*) relationship for individual lithotypes on the rebound-corrected laboratory measurements of *e* (black stars) and (2) by applying the *e*-log(*k*) relationship to the predicted *e* profile (orange line) (Table **T3,** p. 32). Often the predicted *e* overestimates the measured *e*, and thus serves as an upper bound to sediment permeability. For Unit III, an upper and lower permeability were determined by applying the *e*-log(*k*) relationship from Samples 207-1257C-6R-3, 140 cm, and 207-1258B-36R-2, 45 cm. Blue shading represents a qualitative estimate for the possible range of hydraulic conductivity within each lithologic unit.

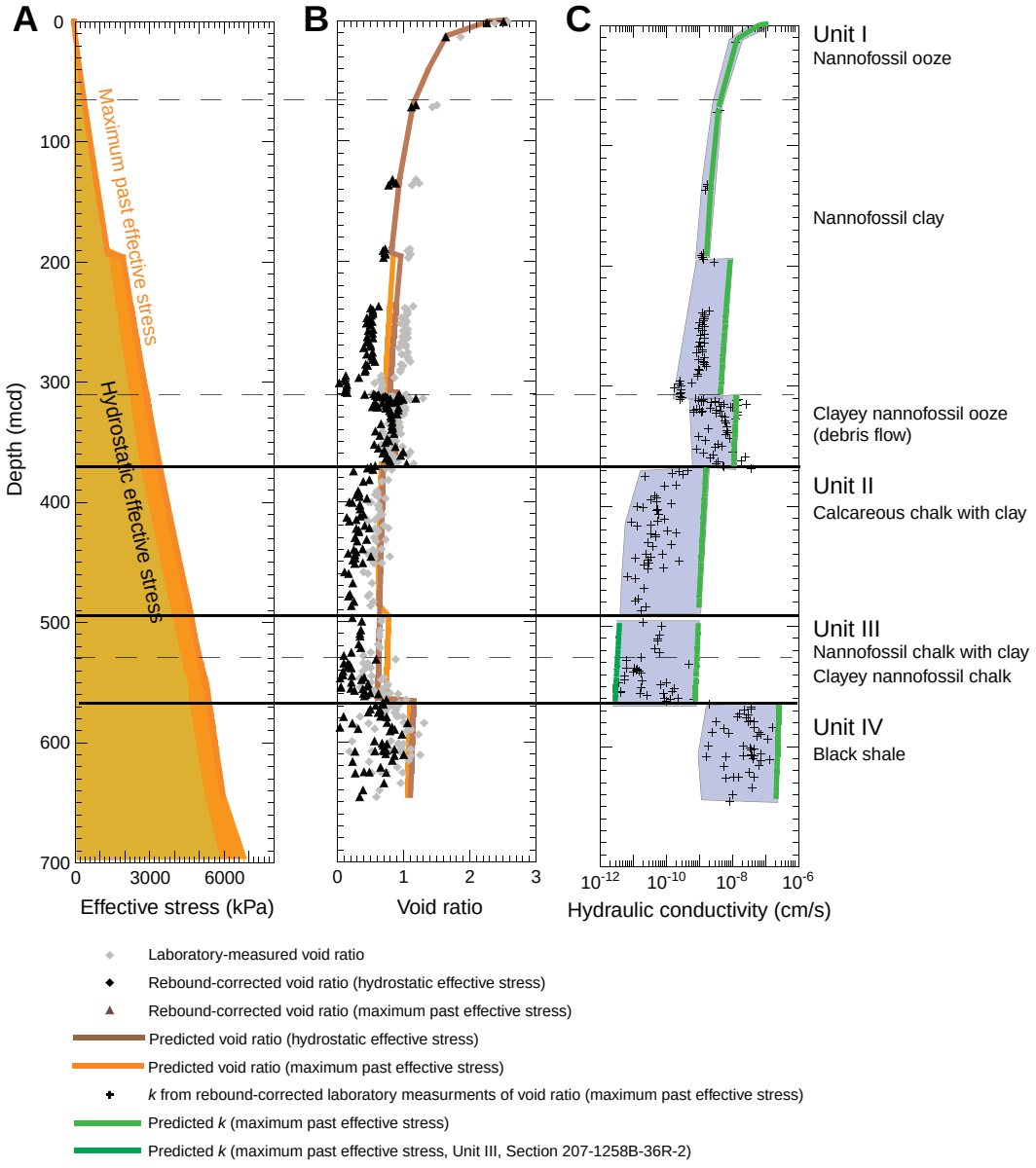

Table T1. Summary of laboratory consolidation results.

Hole, core, section, interval (cm)	Test device	Depth (mbsf)	Depth (mcd)	Initial sample void ratio	Specific gravity (G_s)	Lith. unit	Age	Description	In situ σ′ (kPa)	P_c' (kPa)	OCR	C_c	C_r	e_o	$P_c' - \sigma'$ (kPa)	$P_c' - \sigma'$ (m)*	OCR_m
207-																	
1257C-1R-2, 140	LT	84.90	84.90	1.87	2.70	IIB	early Oligocene–early Eocene	Siliceous nannofossil chalk with foraminifers	490	2000	4.08	1.03	0.04	5.18	1510	246	
1257C-6R-3, 140	LT	134.50	135.70	0.97	2.63	IIIA	late–middle Paleocene	Nannofossil chalk, foram nannofossil chalk	850	1850	2.18	0.36	0.08	1.97	1000	163	
1257C-13R-1, 130	LT	198.60	201.15	1.78	2.33	IV	Cretaceous	Black shale	1330	1850	1.39	1.01	0.07	4.91	520	85	0.72
1257C-16R-5, 135	LT	233.55	234.71	0.74	2.79	V	middle–late Albian	Silty calcareous claystone	1575	550	0.35	0.29	0.08	1.48	–1025	–167	0.19
1258B-36R-2, 8	LA	331.68	344.49	1.12	2.70	III	Maastrichtian	Nannofossil chalk with forams	2575	2750	1.07	0.70	0.12	3.37	175	28	
1258B-45R-4, 45	LA	401.21	422.04	1.20	2.35	IV	Cretaceous	Black shale	3240	1250	0.39	0.45	0.05	2.53	–1990	–324	
1259A-3R-5, 127	LT	25.57	25.57	2.20	2.74	IA	early Miocene, slumped Oligocene	Foram nannofossil ooze	140	450	3.21	0.88	0.09	4.08	310	50	
1261A-4R-2, 90	LT	72.10	72.10	1.48	2.78	IB	middle Pliocene–late Miocene	Nannofossil clay	450	250	0.56	0.67	0.12	2.94	–200	–33	
1261A-4R-2, 90 B	LA	72.10	72.10	1.60	2.78	IB	middle Pliocene–late Miocene	Nannofossil clay	450			0.83	0.18	3.54			
1261A-6R-6, 134	LA	197.95	197.95	1.19	2.70	IB	middle Pliocene–late Miocene	Nannofossil clay	1400	1550	1.11	0.80	0.18	3.54	150	24	
1261A-9R-5, 139	LA	263.59	263.59	1.16	2.68	IB	middle Pliocene–late Miocene	Nannofossil clay	1935	2600	1.34	0.76	0.17	3.42	665	108	
1261A-13R-4, 140	LT	300.60	300.60	1.04	2.50	IB	middle Pliocene–late Miocene	Nannofossil clay	2245	2400	1.07	0.58	0.12	2.78	155	25	
1261A-20R-1, 140	LT	363.50	363.50	0.99	2.73	IC	late Miocene	Clayey nannofossil ooze	2775	2900	1.05	0.26	0.03	1.81	125	20	

Notes: Lith. = lithostratigraphic. * = assuming mean density of 1.65 g/cm^3. LT = Geocomp Loadtrack testing apparatus, LA = lever arm testing apparatus. σ′ = effective stress, P_c' = preconsolidation pressure, OCR = overconsolidation ratio, C_c = compression index, C_r = recompression index, e_o = initial void ratio, OCR_m = modified OCR.

Table T2. Lunne's criteria for evaluating sample disturbance from consolidation test results.

OCR	Very good to excellent	Good to fair	Poor	Very poor
2–4	<4	4–7	7–14	>14
1–2	<3	3–5	5–10	>10

Notes: Lunne's criteria from Lunne et al. (1999). Sample quality is determined by evaluating the volumetric strain (percent) that occurs prior to reaching the preconsolidation pressure during consolidation testing. OCR = overconsolidation ratio.

Table T3. Summary of derived and measured hydraulic conductivity results.

Hole, core, section	σ′ (kPa)	*e* start of load	*e* end of load	Average *e*	C_v (cm^2/s)	A_v (m^2/N)	Derived *k* (cm/s)	Measured *k* (cm/s)	Ratio	Slope	Intercept
207-											
1257C-1R-2	2093	1.77	1.73	1.75	1.57E–04	7.81E–08	4.46E–10	1.78E–07	398.9	1.29	–8.98
	3140	1.73	1.59	1.66	1.50E–03	1.35E–07	7.65E–09	1.19E–07	15.6		
	4186	1.59	1.45	1.52	4.79E–04	1.35E–07	2.57E–09	8.29E–08	32.2		
	6280	1.45	1.26	1.35	8.43E–04	9.28E–08	3.34E–09	4.33E–08	13.0		
	8374	1.26	1.12	1.19	1.08E–04	6.33E–08	3.15E–10	2.95E–08	93.9		
1257C-6R-3	1036	0.83	0.81	0.82	7.62E–04	8.38E–08	3.52E–09	4.39E–09	1.2	3.90	–11.58
	1554	0.81	0.79	0.80	1.32E–03	5.24E–08	3.87E–09	3.00E–09	0.8		
	2072	0.79	0.76	0.77	4.62E–04	4.83E–08	1.26E–09	2.25E–09	1.8		
	3109	0.76	0.71	0.74	6.97E–04	4.87E–08	1.96E–09	1.29E–09	0.7		
	4145	0.71	0.67	0.69	2.94E–04	4.29E–08	7.49E–10	1.27E–09	1.7		
	6281	0.67	0.62	0.64	1.60E–03	2.53E–08	2.47E–09				
	8290	0.62	0.53	0.58	9.23E–05	4.11E–08	2.42E–10				
1257C-13R-1	2049	1.51	1.45	1.48	2.77E–03	1.30E–07	1.48E–08	9.50E–07	64.0	1.98	–8.92
	3073	1.45	1.35	1.40	4.63E–03	9.60E–08	1.86E–08	5.12E–07	27.6		
	4098	1.35	1.25	1.30	3.04E–04	9.10E–08	1.21E–09	3.28E–07	271.3		
	6147	1.25	1.08	1.17	2.11E–03	8.70E–08	8.50E–09	1.71E–07	20.2		
	8196	1.08	0.95	1.01	1.46E–04	6.20E–08	4.52E–10	1.18E–07	261.5		
1257C-16R-5	1554	0.59	0.54	0.56	9.52E–03	7.82E–08	4.78E–08			3.46	–10.52
	2073	0.54	0.51	0.53	1.94E–04	7.05E–08	9.01E–10	1.25E–09	1.4		
	3108	0.51	0.46	0.48	1.83E–04	4.21E–08	5.22E–10	1.47E–09	2.8		
	4145	0.46	0.43	0.45	9.81E–05	3.00E–08	2.04E–10	1.37E–09	6.7		
	6217	0.43	0.37	0.40	6.95E–05	2.77E–08	1.38E–10	4.28E–10	3.1		
	8290	0.37	0.33	0.35	1.34E–04	1.91E–08	1.90E–10				
1258B-36R-2	2582	1.00	0.95	0.98	3.78E–04	6.92E–09	1.33E–10			5.88	–15.26
	3785	0.95	0.90	0.93	8.09E–04	4.25E–09	1.79E–10				
	5482	0.90	0.80	0.85	7.48E–04	6.20E–09	2.52E–10				
	6635	0.80	0.71	0.75	1.53E–05	7.53E–09	6.61E–12				
	8030	0.71	0.59	0.65	7.74E–06	6.97E–09	3.28E–12				
1258B-45R-4	6140	0.89	0.82	0.86	2.26E–08	1.42E–03	1.74E–09				
	7140	0.82	0.80	0.81	3.22E–08	4.72E–04	8.36E–10				
	8200	0.80	0.77	0.79	5.87E–09	9.95E–05	3.22E–11	1.67E–07			
1259A-3R-5	246	1.89	1.83	1.86	1.15E–02	6.50E–07	2.62E–07			1.29	–8.19
	369	1.83	1.75	1.79	9.03E–03	7.10E–07	2.31E–07	1.27E–06	5.5		
	553	1.75	1.64	1.69	5.23E–03	5.60E–07	1.09E–07	8.27E–07	7.6		
	1107	1.64	1.43	1.54	9.15E–03	3.85E–07	1.40E–07	4.02E–07	2.9		
	2214	1.43	1.16	1.29	7.62E–03	2.48E–07	8.27E–08	1.99E–07	2.4		
	4428	1.16	0.85	1.00	5.87E–03	1.37E–07	4.02E–08	8.47E–08	2.1		
1261A-4R-2	400	1.25	1.20	1.22	9.38E–04	5.50E–07	2.33E–08			1.50	–9.69
	500	1.20	1.13	1.16	4.12E–04	7.10E–07	1.36E–08				
	750	1.13	1.03	1.08	3.13E–04	4.16E–07	6.29E–09				
	1000	1.03	0.95	0.99	2.39E–04	3.04E–07	3.66E–09				
	2000	0.95	0.72	0.84	5.01E–04	2.38E–07	6.52E–09				
	3000	0.72	0.62	0.67	3.62E–04	1.06E–07	2.31E–09				
1261A-4R-2 B	1274	1.13	0.96	1.05	2.47E–04	3.11E–07	3.77E–09	2.56E–09	0.7	1.09	–9.66
	2582	0.96	0.75	0.86	3.60E–04	1.65E–07	3.20E–09	1.29E–09	0.4		
	5482	0.75	0.39	0.57	2.50E–04	1.28E–07	2.04E–09	5.92E–10	0.3		
1261A-6R-6	1824	0.97	0.91	0.94	1.42E–03	1.10E–07	8.11E–09	3.50E–09	0.4	1.16	–9.74
	2582	0.91	0.81	0.86				2.81E–09			
	3785	0.81	0.68	0.75	4.51E–04	1.08E–07	2.81E–09	1.67E–09	0.6		
	5482	0.68	0.52	0.60	3.08E–04	9.58E–08	1.85E–09	1.31E–09	0.7		
1261A-9R-5	2582	0.88	0.82	0.85	8.61E–04	8.45E–08	3.94E–09	2.98E–09	0.8	0.99	–9.37
	3785	0.82	0.71	0.77	3.85E–04	9.33E–08	2.05E–09	2.44E–09	1.2		
	5400	0.71	0.57	0.64	3.35E–04	8.51E–08	1.74E–09	1.15E–09	0.7		
	8030	0.57	0.20	0.39		1.49E–07		7.44E–10			
1261A-13R-4	4145	0.75	0.70	0.72	9.27E–04	4.80E–08	2.58E–09				
	6218	0.70	0.60	0.65	7.71E–04	4.80E–08	2.24E–09				
	8290	0.60	0.52	0.56	4.45E–04	3.60E–08	1.03E–09				
1261A-20R-1	4145	0.87	0.85	0.86	8.35E–03	1.60E–08	7.23E–09				
	6218	0.85	0.81	0.83	9.62E–03	1.90E–08	1.00E–08				
	8290	0.81	0.77	0.79	4.05E–03	2.00E–08	4.51E–09				

Note: σ′ = effective stress, *e* = void ratio, C_v = coefficient of consolidation, A_v = slope of the load-displacement curve, *k* = hydraulic conductivity.

Table T4. Summary of low-gradient flow pump results and *k* calculations. (See table note. Continued on next two pages.)

Hole, core, section	Stress (kPa)	Sample height (mm)	Cross-sectional area (cm^2)	q (cm^3/s)	Hydraulic gradient, *i*	*k* (cm/s)	Slope (q-*i*)	R^2	*k* from slope (cm/s)
207-									
1257C-1R-2	2093	20.28	19.35	–4.34E–05	–12.9	–1.76E–07	3.44E–06	0.999	1.78E–07
		20.28	19.35	4.34E–05	11.2	2.03E–07			
		20.28	19.35	–9.45E–05	–29.5	–1.68E–07			
		20.28	19.35	9.45E–05	25.9	1.91E–07			
	3140	19.98	19.35	4.34E–05	14.7	1.55E–07	2.31E–06	1.000	1.19E–07
		19.98	19.35	–4.34E–05	–19.6	–1.16E–07			
		19.98	19.35	9.45E–05	39.8	1.24E–07			
		19.98	19.35	–9.45E–05	–42.0	–1.18E–07			
		19.98	19.35	1.89E–04	80.7	1.23E–07			
		19.98	19.35	–1.89E–04	–84.0	–1.18E–07			
	4186	18.94	19.35	1.93E–05	10.6	9.51E–08	1.60E–06	0.998	8.29E–08
		18.94	19.35	–1.93E–05	–12.4	–8.16E–08			
		18.94	19.35	4.34E–05	23.7	9.56E–08			
		18.94	19.35	–4.34E–05	–25.7	–8.83E–08			
		18.94	19.35	9.45E–05	60.0	8.24E–08			
		18.94	19.35	–9.45E–05	–60.0	–8.24E–08			
	6280	17.91	19.35	–1.93E–05	–28.5	–3.54E–08	8.37E–07	0.995	4.33E–08
		17.91	19.35	1.93E–05	23.0	4.38E–08			
		17.91	19.35	–4.34E–05	–44.4	–5.11E–08			
		17.91	19.35	4.34E–05	43.7	5.19E–08			
		17.91	19.35	–9.45E–05	–114.5	–4.32E–08			
		17.91	19.35	9.45E–05	115.9	4.26E–08			
	8375	16.49	19.35	–1.93E–05	–36.1	–2.79E–08	5.71E–07	0.996	2.95E–08
		16.49	19.35	1.93E–05	38.1	2.65E–08			
		16.49	19.35	–4.34E–05	–68.7	–3.31E–08			
		16.49	19.35	9.52E–06	17.3	2.88E–08			
		16.49	19.35	–9.52E–06	–15.7	–3.16E–08			
		16.49	19.35	4.34E–05	79.6	2.85E–08			
1257C-6R-3	1036	18.54	19.35	9.52E–06	115.4	4.26E–09	8.50E–08	0.991	4.39E–09
		18.54	19.35	3.94E–06	47.8	4.26E–09			
		18.54	19.35	–9.52E–06	–100.6	4.89E–09			
		18.54	19.35	–3.94E–06	–57.9	3.52E–09			
	1554	18.29	19.35	–3.94E–06	–68.1	2.99E–09	5.81E–08	1.000	3.00E–09
		18.29	19.35	3.94E–06	67.6	3.01E–09			
	2072	18.03	19.35	–3.94E–06	–96.0	2.12E–09	4.36E–08	0.987	2.25E–09
		18.03	19.35	3.94E–06	83.2	2.45E–09			
		18.03	19.35	–1.97E–06	–53.3	1.91E–09			
		18.03	19.35	1.97E–06	34.4	2.96E–09			
	3109	17.66	19.35	–3.94E–06	141.9	–1.43E–09	2.49E–08	0.989	1.29E–09
		17.66	19.35	3.94E–06	–174.4	–1.17E–09			
		17.66	19.35	–1.97E–06	72.4	–1.41E–09			
	4145	17.19	19.35	–3.94E–06	171.9	–1.18E–09	2.46E–08	0.994	1.27E–09
		17.19	19.35	3.94E–06	–147.1	–1.38E–09			
1257C-13R-1	2047	17.87	25.55	–1.89E–04	–8.6	8.56E–07	2.43E–05	0.995	9.51E–07
		17.87	25.55	1.89E–04	9.0	8.18E–07			
		17.87	25.55	–4.39E–04	–18.2	9.46E–07			
		17.87	25.55	4.39E–04	16.9	1.02E–06			
	3072	17.27	25.55	–9.45E–05	–7.7	4.83E–07	1.31E–05	0.997	5.13E–07
		17.27	25.55	9.45E–05	6.1	6.04E–07			
		17.27	25.55	–1.89E–04	–13.4	5.51E–07			
		17.27	25.55	1.89E–04	15.5	4.76E–07			
		17.27	25.55	–4.39E–04	–35.0	4.90E–07			
	4096	16.58	25.55	9.45E–05	9.9	3.72E–07	8.38E–06	0.992	3.28E–07
		16.58	25.55	–9.45E–05	–10.8	3.42E–07			
		16.58	25.55	1.89E–04	22.9	3.22E–07			
		16.58	25.55	–1.89E–04	–22.9	3.23E–07			
		16.58	25.55	4.39E–04	42.2	4.07E–07			
		16.58	25.55	–4.39E–04	–53.1	3.24E–07			
	6144	15.60	25.55	9.45E–05	19.1	1.93E–07	4.38E–06	0.985	1.71E–07
		15.60	25.55	–9.45E–05	–20.9	1.77E–07			
		15.60	25.55	1.89E–04	36.5	2.02E–07			
		15.60	25.55	–1.89E–04	–50.4	1.47E–07			
		15.60	25.55	–4.34E–05	–7.5	2.25E–07			
	8192	14.51	25.55	–9.45E–05	–33.2	1.11E–07	3.02E–06	0.990	1.18E–07
		14.51	25.55	4.34E–05	12.3	1.38E–07			
		14.51	25.55	–4.34E–05	–10.3	1.65E–07			

Table T4 (continued).

Hole, core, section	Stress (kPa)	Sample height (mm)	Cross-sectional area (cm^2)	q (cm^3/s)	Hydraulic gradient, *i*	*k* (cm/s)	Slope (q-*i*)	R^2	*k* from slope (cm/s)
		14.51	25.55	9.45E–05	31.5	1.17E–07			
1257C-16R-5	2073	17.54	19.35	3.94E–06	113.4	1.79E–09	2.41E–08	0.976	1.25E–09
		17.54	19.35	–3.94E–06	–269.1	7.57E–10			
		17.54	19.35	9.52E–06	284.4	1.73E–09			
	3108	17.06	19.35	3.94E–06	116.6	1.75E–09	2.84E–08	0.998	1.47E–09
		17.06	19.35	–3.94E–06	–157.1	1.30E–09			
		17.06	19.35	9.52E–06	322.5	1.53E–09			
	4145	16.62	19.35	3.94E–06	168.0	1.21E–09	2.65E–08	0.998	1.37E–09
		16.62	19.35	–9.52E–06	–344.7	1.43E–09			
	6217	16.09	19.35	3.94E–06	475.2	4.28E–10			
1258B-45R-4	6144	16.62	25.55	4.39E–04	0.6	3.09E–05	1.58E–03	0.929	6.19E–05
		16.62	25.55	–4.39E–04	–0.1	1.25E–04			
		16.62	25.55	1.06E–03	0.9	4.71E–05			
		16.62	25.55	–1.06E–03	–0.4	1.09E–04			
		16.62	25.55	2.14E–03	2.6	3.17E–05			
	7140	16.41	25.55	2.14E–03	3.7	2.27E–05	6.31E–04	0.999	2.47E–05
		16.41	25.55	–2.14E–03	–3.0	2.75E–05			
		16.41	25.55	4.19E–03	6.1	2.68E–05			
		16.41	25.55	–4.19E–03	–7.3	2.24E–05			
		16.41	25.55	2.05E–02	32.3	2.49E–05			
	8100	16.10	25.55	1.89E–04	4.9	1.52E–06	3.79E–05	0.997	1.49E–06
		16.10	25.55	–1.89E–04	–4.8	1.54E–06			
		16.10	25.55	4.39E–04	10.7	1.60E–06			
		16.10	25.55	–4.39E–04	–12.5	1.38E–06			
1259A-3R-5	360	17.52	19.35	9.45E–05	3.0	1.65E–06	2.48E–05	0.959	1.28E–06
		17.52	19.35	–9.45E–05	–5.1	9.64E–07			
		17.52	19.35	1.89E–04	10.1	9.70E–07			
		17.52	19.35	–1.89E–04	–11.2	8.71E–07			
		17.52	19.35	4.39E–04	15.7	1.44E–06			
		17.52	19.35	–4.39E–04	–15.2	1.50E–06			
	540	16.91	19.35	4.34E–05	2.4	9.31E–07	1.62E–05	0.998	8.37E–07
		16.91	19.35	–4.34E–05	–2.3	9.84E–07			
		16.91	19.35	9.45E–05	6.1	8.02E–07			
		16.91	19.35	–9.45E–05	–5.6	8.74E–07			
		16.91	19.35	1.89E–04	12.0	8.13E–07			
		16.91	19.35	–1.89E–04	–11.4	8.58E–07			
	1080	15.67	19.35	–4.34E–05	–4.0	5.65E–07	7.88E–06	0.998	4.07E–07
		15.67	19.35	4.34E–05	4.8	4.65E–07			
		15.67	19.35	–9.45E–05	–11.7	4.16E–07			
		15.67	19.35	9.45E–05	12.2	4.00E–07			
		15.67	19.35	–1.89E–04	–24.0	4.07E–07			
		15.67	19.35	1.89E–04	24.3	4.01E–07			
	2160	14.10	19.35	4.34E–05	10.8	2.07E–07	3.90E–06	0.997	2.02E–07
		14.10	19.35	–4.34E–05	–9.3	2.41E–07			
		14.10	19.35	9.45E–05	26.6	1.84E–07			
		14.10	19.35	–9.45E–05	–21.8	2.24E–07			
		14.10	19.35	1.89E–04	49.3	1.98E–07			
		14.10	19.35	–1.89E–04	–47.9	2.04E–07			
	4320	12.48	19.35	1.93E–05	12.5	8.01E–08	1.66E–06	0.992	8.58E–08
		12.48	19.35	–1.93E–05	–7.9	1.27E–07			
		12.48	19.35	–4.34E–05	–20.5	1.10E–07			
		12.48	19.35	4.34E–05	23.6	9.51E–08			
		12.48	19.35	–9.45E–05	–56.5	8.64E–08			
		12.48	19.35	9.45E–05	60.4	8.09E–08			
1261A-4R-2 B	472	17.03	19.35	9.52E–06	68.8	7.88E–09	1.13E–07	0.993	5.82E–09
		17.03	19.35	–9.52E–06	–69.6	7.79E–09			
		17.03	19.35	9.52E–06	77.2	7.02E–09			
		17.03	19.35	–3.94E–06	–32.0	7.00E–09			
		17.03	19.35	1.93E–05	159.2	6.90E–09			
		17.03	19.35	–1.93E–05	–164.7	6.67E–09			
		16.41	19.35	–1.93E–05	–204.8	5.17E–09			
	722	16.41	19.35	1.93E–05	200.2	5.29E–09	8.47E–08	0.975	4.38E–09
		16.41	19.35	–9.52E–06	–106.2	4.92E–09			
		16.41	19.35	3.94E–06	41.9	5.16E–09			
		16.41	19.35	9.52E–06	123.0	4.24E–09			
		15.11	19.35	9.52E–06	161.3	2.98E–09			
	1274	15.11	19.35	–9.52E–06	–209.8	2.29E–09	4.30E–08	0.841	2.22E–09
		15.11	19.35	3.94E–06	82.7	2.41E–09			

Table T4 (continued).

Hole, core, section	Stress (kPa)	Sample height (mm)	Cross-sectional area (cm^2)	q (cm^3/s)	Hydraulic gradient, *I*	*k* (cm/s)	Slope (q-*i*)	R^2	*k* from slope (cm/s)
		15.11	19.35	–9.52E–06	–84.1	5.72E–09			
		13.48	19.35	–3.94E–06	–139.5	1.27E–09			
	2582	13.48	19.35	3.94E–06	144.9	1.23E–09	2.63E–08	0.984	1.36E–09
		13.48	19.35	–1.97E–06	–64.9	1.37E–09			
		10.67	19.35	1.97E–06	110.9	6.34E–10			
	5486	10.67	19.35	–1.97E–06	–104.8	6.71E–10	1.31E–08	0.974	6.76E–10
		10.67	19.35	–2.96E–06	–224.1	4.71E–10			
1261A-6R-6	1821	17.70	19.35	–3.94E–06	–56.8	3.58E–09	6.76E–08	0.999	3.50E–09
		17.70	19.35	3.94E–06	57.0	3.57E–09			
		17.70	19.35	–9.52E–06	–145.9	3.37E–09			
		17.70	19.35	9.52E–06	136.5	3.61E–09			
	2582	16.98	19.35	3.94E–06	73.0	2.79E–09	5.45E–08	1.000	2.81E–09
		16.98	19.35	–3.94E–06	–78.3	2.60E–09			
		16.98	19.35	9.52E–06	171.3	2.87E–09			
		16.98	19.35	–9.52E–06	–175.4	2.81E–09			
	3785	15.95	19.35	–3.94E–06	–95.3	2.14E–09	3.23E–08	0.996	1.67E–09
		15.95	19.35	3.94E–06	128.5	1.58E–09			
		15.95	19.35	–9.52E–06	–266.6	1.85E–09			
		15.95	19.35	9.52E–06	276.7	1.78E–09			
		15.95	19.35	–1.93E–05	–616.5	1.62E–09			
	5482	14.63	19.35	3.94E–06	131.3	1.55E–09	2.53E–08	0.995	1.31E–09
		14.63	19.35	–3.94E–06	–186.2	1.09E–09			
		14.63	19.35	9.52E–06	351.4	1.40E–09			
		14.63	19.35	1.97E–06	97.1	1.05E–09			
		14.63	19.35	–1.97E–06	–88.5	1.15E–09			
1261A-9R-5	2582	17.16	19.35	3.94E–06	65.4	3.11E–09	5.76E–08	0.998	2.98E–09
		17.16	19.35	–3.94E–06	–65.6	3.10E–09			
		17.16	19.35	9.52E–06	156.2	3.15E–09			
		17.16	19.35	–9.52E–06	–175.8	2.80E–09			
	3785	16.38	19.35	–3.94E–06	–103.4	1.97E–09	4.72E–08	0.974	2.44E–09
		16.38	19.35	3.94E–06	97.8	2.08E–09			
		16.38	19.35	–9.52E–06	–177.6	2.77E–09			
	5482	15.22	19.35	3.94E–06	173.4	1.17E–09	2.23E–08	1.000	1.15E–09
		15.22	19.35	–3.94E–06	–180.1	1.13E–09			
	8096	12.87	19.35	2.76E–06	176.6	8.07E–10	1.44E–08	0.996	7.44E–10
		12.87	19.35	–1.97E–06	–143.1	7.11E–10			
		12.87	19.35	1.97E–06	145.1	7.01E–10			

Note: q = flow rate, *k* = hydraulic conductivity.